NDT&E International 128 (2022) 102626

Contents lists available at ScienceDirect

NDT and E International

journal homepage: www.elsevier.com/locate/ndteint

A Bayesian approach for damage assessment in welded structures using Lamb-wave surrogate models and minimal sensing

Mohammad Ali Fakih [a,b], Manuel Chiachío [c,d,*], Juan Chiachío [c,d], Samir Mustapha [b,**]

[a] Institute of Fluid-Flow Machinery, Polish Academy of Sciences, 80-231, Gdańsk, Poland
[b] Laboratory of Smart Structures and Structural Integrity (SSSI), Department of Mechanical Engineering, American University of Beirut, Beirut, Lebanon
[c] Department of Structural Mechanics and Hydraulic Engineering, University of Granada (UGR), Granada, 18001, Spain
[d] Andalusian Research Institute in Data Science and Computational Intelligence (DaSCI), Granada, 18071, Spain

ARTICLE INFO

Keywords:
Structural health monitoring
Lamb waves
Dissimilar joints
Bayesian inverse problem
Surrogate modelling
Artificial neural network

ABSTRACT

The increasing mechanical and economical demands in modern systems and structures are forcing an inevitable need for joining dissimilar materials, thus creating the challenge of establishing a process to inspect and monitor dissimilar joints. Condition monitoring is a necessity to ensure that the structures are being safely used and to extend their lifetime. Lamb waves (LWs) are ultrasonic guided waves that are widely used for structural health monitoring of mechanical, aerospace, and civil structures. This paper proposes a novel structural health monitoring approach for damage detection, localization, and assessment using a minimal LW sensor-actuator set-up. More specifically, the proposed framework provides damage detection, localization and assessment within a dissimilar-material joint by Bayesian inference of six parameters of damage extent and location. Finite element simulations are used to simulate the measured LWs and generate a dataset required to train artificial neural networks (ANN), acting as surrogate models for LW simulation with reduced computational cost. The ANN-based LW simulations are further used as forward model within an Approximate Bayesian Computation (ABC) framework to provide probabilistic inference of the damage size and position. The results show that damage of different sizes and locations can be successfully identified with a high level of resolution and with quantified uncertainty. The results also show that data fusion for ABC inference using multiple sensor measurements can be possible with improved inference results. However, a precise and robust damage inference can be achieved using a minimal sensing set-up based on one actuator and two sensing points, with consideration of certain levels of measurement noise. These findings imply a considerable reduction of complexity of LW actuator-sensor networks, and overall, they imply a significant reduction of computational resources and cost for damage detection and assessment in structures, thus providing a step forward towards online/onboard monitoring applications.

1. Introduction

The increasing demand for higher fuel efficiency in all kinds of mobile vehicles has led to a greater interest in using lightweight materials in their structures [1,2]. Variants of aluminum and magnesium alloys are being widely used in transportation and aerospace industries due to their lightweight and attractive properties, including high specific strength, corrosion resistance, and good formability [1,3]. Using different materials in specific locations of structures is an advantageous strategy to optimize designs from both mechanical and economical perspectives by fully exploiting the materials' native properties (e.g., mechanical, thermal, physical, chemical, etc.) [2,4]. In such a case, dissimilar joints between different metallic alloys become a need, however they require effective technological solutions to guarantee their structural integrity. Invisible or buried defects within welded regions, if remained undetected, may develop into bigger cracks, compromising the safety of the whole structure, and leading to catastrophic failures [5].

During more than three decades, *structural health monitoring* (SHM) technologies have been developed and used for the early detection of structural damage to prevent sudden failures [6]. Within them, the use of ultrasonic guided waves, and especially Lamb waves (LWs) [7–9], has

* Corresponding author. Department of Structural Mechanics and Hydraulic Engineering, University of Granada (UGR), Granada, 18001, Spain.
** Corresponding author. Laboratory of Smart Structures and Structural Integrity (SSSI), Department of Mechanical Engineering, American University of Beirut, Beirut, Lebanon.
E-mail addresses: mchiachio@ugr.es (M. Chiachío), sm154@aub.edu.lb (S. Mustapha).

https://doi.org/10.1016/j.ndteint.2022.102626
Received 26 August 2021; Received in revised form 6 February 2022; Accepted 14 February 2022
Available online 22 February 2022

emerged as a promising solution due to their sensitivity to the existence of various types and sizes of defects [10], their ability to propagate in complex structures and for long distances [11], and their capability to inspect hidden areas [12].

Many challenges still have to be addressed to guarantee a successful implementation and reliable application of SHM systems on real structures. Early damage identification is one of the main objectives that need to be met using a continuous SHM system. The latter includes early damage detection, localization, and assessment [13]. Achieving these three objectives with a minimal number of transducers is of high importance for the industrial community to move the developed technology from research into real life applications.

The design of the sensor network is one of the main bottlenecks for the successful implementation of SHM systems. The research found in the current literature demonstrate that even in an optimized sensor network, a relatively large number of transducers is still required to maximize the coverage. Recent works have contributed on the optimization of sensor networks for damage localization in plate-like structures using LWs excited and received by dual-functional lead zirconate titanate (PZT) transducers. In Refs. [14,15] a total of 14 PZTs were required to ensure a 95% coverage for a plate-like structure of about 500 × 500 [mm^2]. More recently [9], reported the coverage of a large metallic surface of 2740 × 2385 [mm^2] from an Airbus A330 cargo door using 48 PZTs assuming a maximum effective actuator-sensor distance of 1.5 m. Other authors have used the Bayesian information theoretic approach for LW-based sensor-network optimization [16]. Particularly relevant are the works by Cantero-Chinchilla et al. who developed optimization techiques based on the value-of-information [17] and on the convexification of the cost-benefit function [18]. In Ref. [17], 6 transducers (1 actuator and 5 sensors) were needed to ensure decent coverage of a damage area of 200 × 400 [mm^2], whilst in Ref. [18], 6 dual-functional PZTs were shown to be enough to cover a damage area more than five times larger. The referred studies reflect that covering a larger component or sub-component of a structure, like an aircraft wing or a wind turbine blade, would demand the employment of a significant number of PZT transducers. This leads to many challenges in the design and integration of the network, apart from the additional weight and high cost. In the literature, the use of damage indices (DIs) has shown to be an effective solution to tackle with the LW monitoring of large structures using complex sensor-networks [19]. Indeed, some of the authors of this paper [8,10,11] have effectively addressed the damage detection and localization problem based on several DIs for qualitative classification or comparison between several damage severities. However, these studies show that DIs fail on providing a direct quantitative assessment of the damage severity.

The current study aims at the development of a novel technique to deal with the three damage identification objectives, namely detection, localization, and assessment, using a minimal number of transducers. To this end, a model-driven inverse problem methodology embedded within different computational intelligence algorithms, including *Artificial Neural Networks* (ANN) and *Approximate Bayesian Computation* (ABC) [20], is employed. In this work, the model-driven approach is used for damage assessment since it provides information about the underlined physics of the wave propagation and its interaction with the medium [12], which includes the structural discontinuities, the boundaries, and also the damage. Note that these damage models require the use of analytical and numerical methods such as finite element (FE) or semi-analytical finite element (SAFE) models, among others, whereby damage identification can be obtained by systematic comparison to an intact signal, taken as benchmark. However, the latter is at the cost of a high computational demand required per each damage simulation, thus making it impractical for on-line SHM [21].

The current paper addresses the drawbacks mentioned in Ref. [21] by training a LW surrogate model based on previously performed FE simulations, to efficiently replace the FE model during online SHM. The resulting surrogate model can systematically simulate LW signals at a certain sensing point in almost real-time given the damage size and position and with a very low computational cost. This has enabled for the application of Bayesian damage inference which would have been computationally infeasible if the physical model was directly employed. In particular, the ABC by subset simulation, known as ABC-SubSim algorithm [22], is used as Bayesian inference algorithm due to its computational efficiency and accuracy. The algorithm yields probability density functions (PDFs) of the inferred damage parameters as measure of the relative degree of confidence in the possible damage scenarios, considering both measurement and modeling uncertainties. As a result, six damage parameters of size and position can be inferred with quantified uncertainty. Due to the physics-based LW propagation model embedded within the ANN acting as forward simulation in the ABC-SubSim, the damage identification and assessment is provided with significant accuracy using an absolutely minimal actuator-sensor configuration based on one sensor and one actuator within a plate-like area, thus avoiding the use of complex sensing networks to provide the required accuracy. Indeed, the proposed damage identification approach with minimal sensing has also shown robustness against significant measurement noise levels, however the results indicate that the more sensors used the better the robustness. Further, the proposed surrogate modeling approach can cater to different sources of information while training including analytical, numerical, and experimental data; this will lead to a more informed model. The proposed approach would also be helpful in digital twinning applications, where the minimal sensing need is a fundamental preference, and overall, in key industries for the SHM domain like aeronautics and aerospace, where the complexity of the sensing system implies higher weight and extra vulnerabilities.

Similar to the work by Sbarufatti et al. [19], most of the works found in literature use DIs or features extracted from the waves as inputs for the ANN, which in turn is used to predict the damage parameters [23–25]. On the contrary, in this paper the ANN is used to produce the LW simulation with consideration of damage and not to give any damage indicator of damage position and size. Indeed, the inputs of the ANN will be the damage parameters (size and position), producing as output the predicted LW signal.

The proposed methodology is generic, however the approach has been validated in a plate-like area of 250 × 250 [mm^2] with a welded joint between AA6061-T6 aluminum alloy and AZ31B magnesium alloy, ultimately to detect and quantify defects that may exist at the weld line.

The rest of the paper is organized as follows. Section 2 introduces the FE model developed for generating sensor measurements of different damage cases. In Section 3, the ANN-based surrogate modeling of the FE physical model of LW propagation, is presented, which is further used for damage inference by Approximate Bayesian Computation in Section 4. Section 5 presents the results about inference of selected damage cases and provides discussion about the prediction performance. In Section 6, a discussion on the methodology is given, and finally, Section 7 gives concluding remarks.

2. Finite element modeling

The Finite Element Method (FEM) is used as a forward model to obtain physical simulations of LW propagation through a metallic plate, including a dissimilar-material butt-welded joint, under different damage scenarios. The simulations are produced to generate a dataset of synthetic ultrasonic measurements under various damage cases whereby a surrogate model can be further trained to replace the FE model with significantly reduced computational cost.

The physical model, which has been implemented using Abaqus®/CAE commercial software, consists of two AA6061-T6 and AZ31B subplates, sized 250 × 125 × 3 [mm^3], which are joined together assuming a perfect joint, thus forming a welded plate of 250 × 250 × 3 [mm^3] dimensions, as depicted in Fig. 1. Homogeneous isotropic linearly elastic behavior is assumed for the constituent-metallic materials,

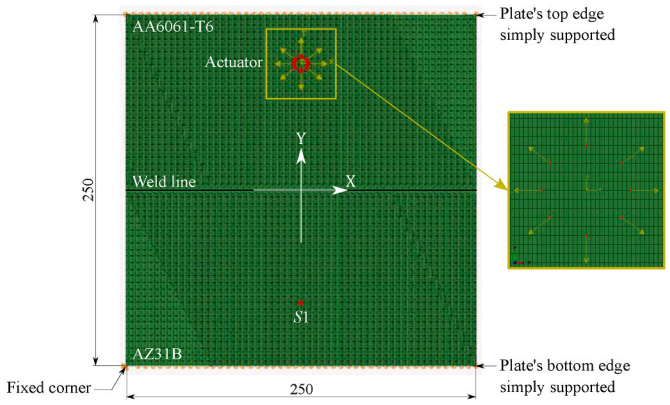

Fig. 1. A view of the FE model showing the actuator model (inset) and the sensing point $S1$ (in red) on the bottom side of the plate. Note that the weld line lies along the X-direction. Dimensions are expressed in [mm]. (For interpretation of the references to color in this figure legend, the reader is referred to the Web version of this article.)

whose physical and mechanical properties are listed in Table 1. The geometry is meshed using linear hexahedral elements with reduced integration through the element type C3D8R, with size $1 \times 0.5 \times 0.5$ [mm^3]. The weld region (corresponding to 5 [mm] before and after the interface) is meshed using an element size of $0.5 \times 0.5 \times 0.5$ [mm^3], which allows enough flexibility to represent a variety of damage extents and positions. This mesh configuration ensures the availability of more than ten elemental-nodes per wavelength in the in-plane dimensions, based on the used excitation frequency, as recommended in the literature for LW FE simulation [26–30]. Moreover, enhanced hourglass control is employed to avoid extreme element deformation upon using reduced integration elements. For the boundary conditions, the edges coinciding with the X-direction on the bottom surface of the plate are simply supported, whilst the lower-left corner is fixed to prevent the model from movement, as labeled on Fig. 1.

Abaqus®/Explicit solver is used to perform the wave simulations of 150 microseconds (μs) each, with a maximum time step of 5×10^{-2} [μs]. A five-cycle Hann-windowed sinusoidal wave of 300 [kHz] central frequency is excited through the plate by feeding radial in-plane point forces to the nodes representing a circular PZT actuator [8]. The actuator, of 10 [mm] diameter, is placed at 90 [mm] center distance from the weld line in the AA6061-T6 sub-plate, with its center located at the YZ-plane. A surface node of 80 [mm] located on the other side of the weld line (in the AZ31B sub-plate), is used as a sensing point and referred to as $S1$. The in-plane displacements in the direction perpendicular to the weld line (U_2, along the Y-axis) and the out-of-plane displacements (U_3, along the Z-axis) are recorded for $S1$ at a sampling rate of 20 [MHz]. The excitation central frequency of 300 [kHz] was chosen based on experimental observations of LWs in similar plates [8,31]. At this frequency, only the fundamental Lamb-wave modes will exist and with a good difference in the group velocity between the symmetric (S_0) and antisymmetric (A_0) modes, according to the theoretical LW dispersion curves [32]. This would provide a good signal quality with well-separated wave packs. As a typical damage type in FSW joints, wormhole damage of rectangular-cuboid shape of variable damage size and position, is assumed to exist within the weld region. In this work, six damage parameters are used to mathematically describe the damage extent and position, namely, length (ℓ), width (w), and thickness (t), along with the coordinate positions x, y, and z, respectively. Fig. 2 illustrates a damage example with indication of the size and position parameters. Note that the $\{x, y, z\}$ positions are considered as the coordinates of the center of the damage with respect to the center of the plate. The damage is added to the model by deleting the damaged elements from the FEM mesh before submitting the modified file for simulation. In this work, numerous (i.e., thousands) damage cases are simulated, thus the MATLAB® and Abaqus2Matlab MATLAB®-based software [33] are used to automate the modeling, execution, and post-processing of these damage cases in an efficient manner. For ANN training purposes, waves are excited from the AA6061-T6 to the AZ31B sub-plates using a variety of damage parameters, in addition to the intact state of the plate. In the simulations, both the U_2 and U_3 displacement measurements are recorded at the sensing point $S1$, namely U_{2S1} and U_{3S1}. For the simulations, the ranges of damage parameters have been carefully chosen to ensure that the resulting damage cases are good representatives of all possible damage scenarios. Table 2 lists the ranges of variation of the damage parameters along with their variation increments used in this study. In total, 10888 possible damage cases are finally considered as a simulated dataset for ANN training and testing.

Table 1
Physical and mechanical properties of the used materials.

Material	Density [Kg/m^3]	Young's modulus [GPa]	Poisson's ratio
AA6061-T6 aluminum alloy	2700	69	0.33
AZ31B magnesium alloy	1770	45	0.35

3. ANN-based Lamb-wave surrogate modeling

In this section, an ANN-based Lamb-wave surrogate model is proposed as an approximated fast-computing forward model replacing the FE model. The surrogate modeling process is composed of several steps including data preprocessing, balancing, reduction, and splitting, in addition to the ANN design, training, validation, and then testing. These steps will be explained in the following subsections.

3.1. Data preparation

Fig. 3a shows the simulation results of U_{2S1} for both an intact and a damaged weld sample with the following damage parameters, referred to here as D1: $\{\ell = 50, w = 2, t = 1.5, x = 0, y = 0, z = 0.25\}$, where the units are expressed in milimeters. Note that amplitude variations and changes in the signal's shape are evident between the healthy and damaged case. The wave-packs corresponding to the first transmissions of the waves' S_0 and A_0 modes are marked on the figure. They correspond to the waves' S_0 and A_0 modes transmitted directly from the actuator to the sensing point. Modes are identified based on a previous study [34], where a similar model and actuator-sensor configuration were used. Since the S_0 mode is considerably faster than the A_0 mode, A_0's first transmission is mixed with some S_0 boundary reflections, as indicated in the figure. The other wave-packs correspond to waves measured by the sensing point after bouncing from the plate's boundaries, the so-called boundary reflections. Observe that the first transmission of the S_0 mode shows a significant amplitude attenuation due to the presence of the damage within the signal's direct path between the actuator and $S1$, also named as sensing path. Note as well that the boundary reflections are also affected by the presence of the damage.

Similarly, Fig. 3b shows the U_{2S1} measurement comparing the intact weld to another damage case named as D2, of the same size as D1 but located on the left side of the weld, with parameters: $\{\ell = 50, w = 2, t = 1.5, x = -75, y = 0, z = 0.25\}$, expressed in [mm]. Fig. 3b reflects that the first transmission is not affected by the damage, unlike what was seen in the case of D1. This is due to the shift of the damage location from the line of sight. However, the plot reveals that the boundary reflections are affected by the existence of the damage D2. For further emphasis, Fig. 12a will later illustrate two damage cases where the damage does not exist within the coverage of the sensing path, however, it can still be perceived by the sensor when considering the wave's boundary reflections. This preliminary analysis reflects the need to consider the entire signal including both the direct transmissions and

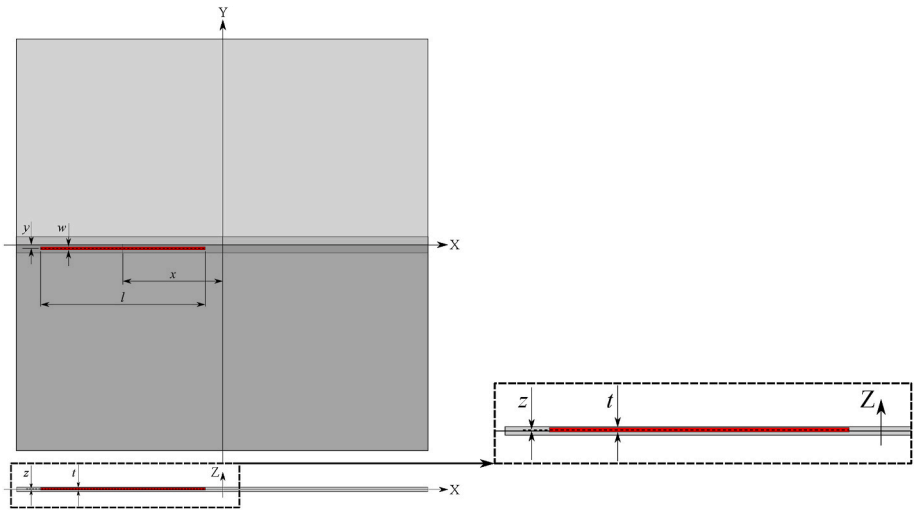

Fig. 2. An illustration showing the welded plate containing a damage example (in red) and the six damage parameters. Position parameters are measured with respect to the center of the damage. (For interpretation of the references to color in this figure legend, the reader is referred to the Web version of this article.)

Table 2
Ranges of the damage parameters used for the simulated damage cases. The third row shows the incremental step per damage parameter.

Damage parameter	ℓ	w	t	x	y	z
Minimum value [mm]	25	1	0.5	−100	−1.25	−1.25
Increment [mm]	25	1	0.5	25	0.25	0.25
Maximum value [mm]	200	3	2.5	100	1.25	1.25

boundary reflections in the current study. Thus, since the entire signal is used for calculations, data preprocessing is required to minimize the computational burden for all the available FE-wave simulations before being used as training or testing units. In this work, data reduction was carried out by three different means: signal cutting, signal down-sampling, and sample reduction, where the latter is explained in Section 3.2. For the signal cutting, 30 [μs] signal segment was cut out from all the start of the signals since it does not carry any useful information, as can be seen in Fig. 3. Further, all the signals were down-sampled from 20 to 3 [MHz] sampling rate. After preprocessing, the length of each signal was reduced from 2999 to 361 data points. Lowering the number of data samples in the signal lowers the size of the ANN's output layer in the same manner and, thus, allows for a less complex ANN architecture. This would not only reduce the training and testing computational cost of the ANN, but would also lead to a much faster surrogate model.

3.2. ANN architecture and training

In ANN training and testing, the overfitting is a typical major drawback which makes the trained model learn the details of the data in such a way that it negatively affects the performance of the model on new data. When over-fitted, the trained model will fit excessively well to the training data such that it would even learn the noise and possible errors of the data [35], and would not fit for a newly presented data, thus giving wrong or inaccurate predictions. This problem is called a generalization problem of the trained model that can happen if the training dataset is not large enough nor carefully chosen to represent the whole population of known and unknown samples. Also when the data are unbalanced in a way that makes the model learn about a part of the population more than it learns about other parts (so-called biased data).

In the current study, the training data come from FE simulations, which cancels the possibility of noisy or outlier data within the training set. Further, the geometry of the monitored structure, which corresponds to the welded region of the plate in this case, makes the universe of all possible damage scenarios finite and well bounded. This makes it easy for the user to define a well balanced and well-distributed training dataset that can be a good representative of the whole population of possible damages. These facts allowed the training of the ANNs down to extremely low performance errors, without the concern of having generalization problems. Fig. 4 displays an illustration of the rationale behind this concept. As mentioned above, 10801 observations were collected for each of the two ANNs, which correspond to 10800 damage cases plus one healthy case. Out of these, 594 damage cases were chosen in a well distributed manner to test the effectiveness of the approach over different ranges of damage sizes and positions. Thus, 10207 cases were kept for training, including one healthy weld case. To balance the training dataset and improve the results for small damages, data measured from the healthy case was made available multiple times within the training dataset but for different virtual damage positions. The healthy measurements were repeated with 1859 different virtual damage positions, according to Table 3, thus increasing the total amount of observations in the training dataset to 12065 cases for each of the two ANNs. Since selecting a random dataset from a large pool would keep a good data balance and distribution, the training dataset was reduced to half through a random sample reduction process. Finally, the training and testing datasets included 6032 and 594 samples, respectively, for each of the two ANNs. The inputs (predictors) of each ANN are the six damage parameters of the wormhole damage lying within the weld, namely $\{\ell, w, t, x, y, z\}$, while the outputs are a set of 361 values representing the data points of the predicted LW signal received at the sensing point $S1$. On that basis, the architecture of the ANN was decided by performing a trial-and-error process in search for a well performing and computationally efficient design. The number of hidden layers as well as the number of neurons in each hidden layer were varied in different combinations, while comparing the signals predicted by the ANN to the FE simulation signals, until satisfactory results were attained. During this process, it was kept in mind that both the training and prediction times would significantly increase when increasing the complexity of the ANN architecture. Finally, an ANN architecture of two 200-neuron hidden layers plus a 361-neuron output layer was adopted, as shown in Fig. 5. The training data were split using the typical ANN design procedure into a training set and a validation set. To ensure good data splitting and better model generalization, *k-fold cross validation* of ten folds [36] was applied. Scaled conjugate gradient backpropagation function [37] was used for training the model, and the performance of the ANN, while training, was evaluated using the mean square error function. To further prevent overfitting, the *maximum validation fails* early stopping criterion was adopted using 1000 as maximum allowed

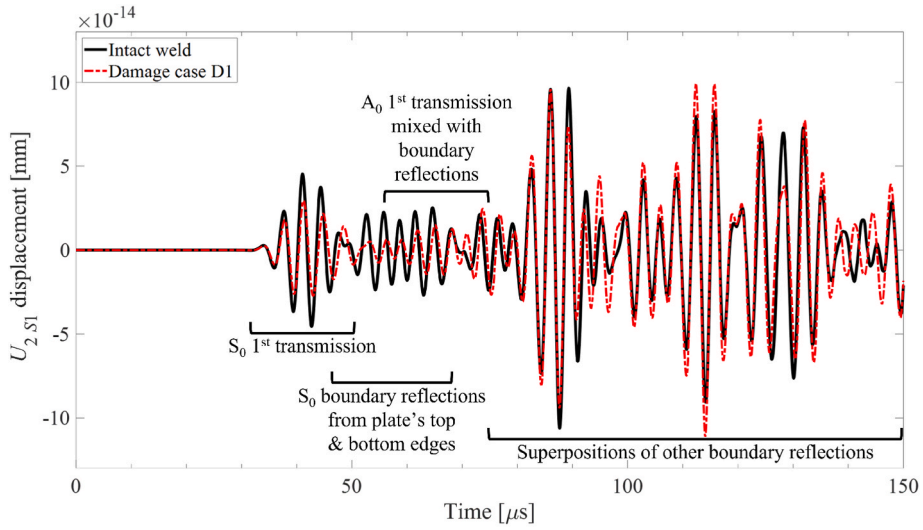

(a) Damage case D1

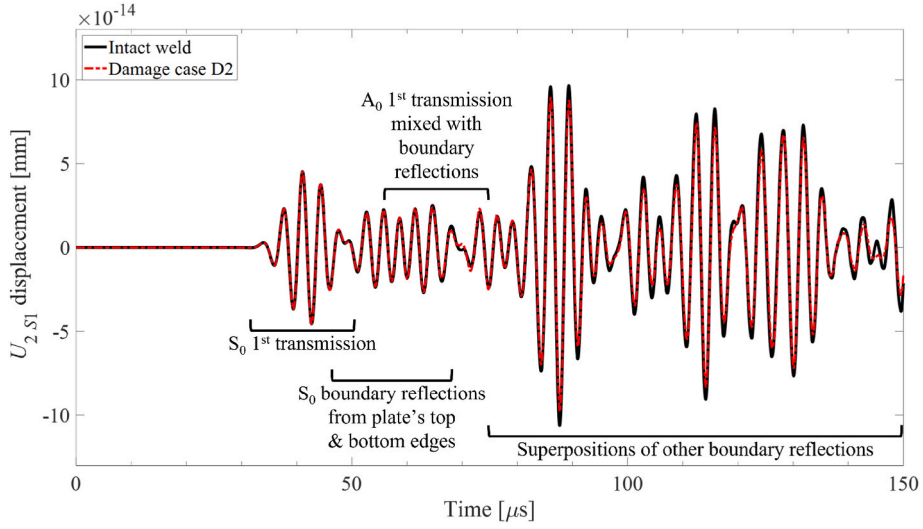

(b) Damage case D2

Fig. 3. Raw signals of U_{2S1} for the intact (black line) and damaged weld (in red). Two damage cases D1 (Panel a) and D2 (Panel b) are considered. D1 lies within the coverage of the sensing path, while damage D2 lies outside the coverage of the sensing path. (For interpretation of the references to color in this figure legend, the reader is referred to the Web version of this article.)

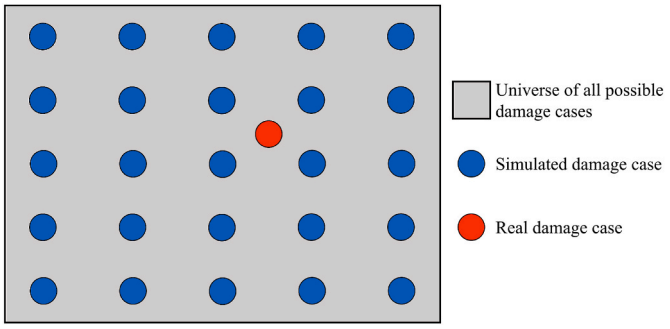

Fig. 4. An illustration showing a well balanced and well distributed training dataset which should be convenient for training down to extremely low performance errors, without generalization concerns when seeing a true damage case.

Table 3
Range of virtual damage positions of the healthy cases added to the training dataset for data balance. In total 1,859 healthy signals are added with different virtual damage positions.

Damage parameter	ℓ	w	t	x	y	z
Minimum value [mm]	0	0	0	−125	−1.5	−1.5
Increment [mm]	0	0	0	25	0.25	0.25
Maximum value [mm]	0	0	0	125	1.5	1.5

fails. The other stopping criteria were relaxed so that the training would not stop except when reaching the maximum validation fails. These criteria include the maximum number of training epochs ($\leqslant 5 \cdot 10^5$), the best performance over the training data (goal $= 10^{-6}$), and the minimum performance gradient (10^{-7}). Finally, to visually check the agreement between the signals predicted by the ANN model and the testing signals, a sample of the ANN prediction for one of the testing damage cases is

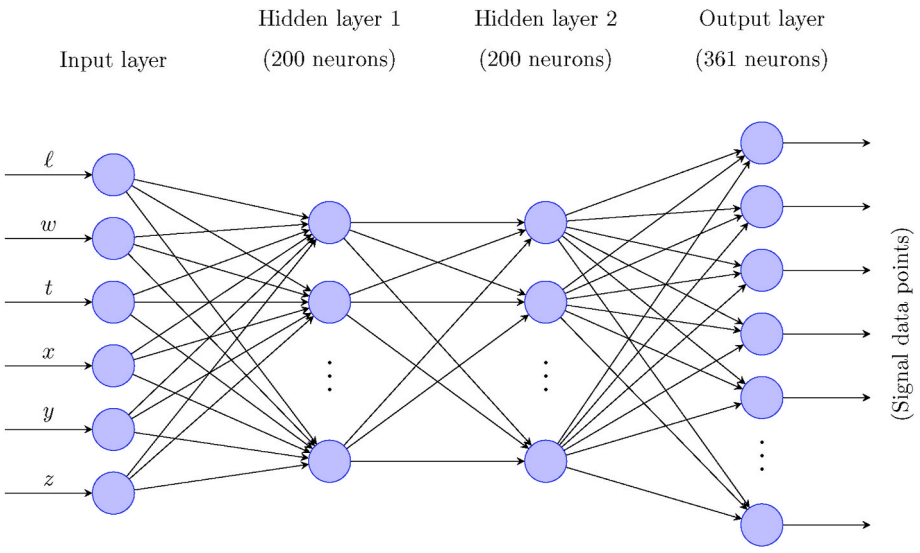

Fig. 5. A schematic illustration of the ANNs used as surrogate models for Lamb-wave measurement prediction.

plotted versus its corresponding testing one in Fig. 6. For this example, the damage parameters were randomly chosen to be (in [mm]): $\{\ell = 25, w = 1, t = 1, x = -75, y = -1, z = -1\}$, referred to as damage case D3. Note that the signals obtained using FE simulation and the ANN for measurement U_{3S1} show good agreement.

4. Damage inference by Approximate Bayesian Computation

This section presents the method for damage parameter inference given one or several sensor measurements and using multiple LW surrogate models (i.e., trained ANNs). To this end, let $\mathcal{D} = \{s \in \mathbb{R}^l\}$ be the set of training data whose elements come from FE simulation, as stated in the previous section. From a frequentist point of view, the damage predictors $\{\ell, w, t, x, y, z\}$ are assumed to be unknown but deterministic values which are revealed through the ANN after training with a dataset $\mathcal{D}$. However, in real-life situations, damage parameters come with an implicit uncertainty about their values, that is not covered by the frequentist approach. Under a Bayesian perspective, the uncertainty about the damage parameters can be considered, and the objective is no longer to obtain the true value of the damage parameters but a distribution of their plausible values in congruence with the training dataset $\mathcal{D}$ [38]. From a mathematical point of view, let $\boldsymbol{\theta} \in \boldsymbol{\Theta} \subset \mathbb{R}^{n_p}$ be the set of model parameters such that $\boldsymbol{\theta} = \{\theta_1, \theta_2, \ldots, \theta_6\} \equiv \{\ell, w, t, x, y, z\}$, thus $n_p = 6$. Next, let us denote by $\widehat{s} = f(\boldsymbol{\theta}, \mathbf{u}) \in \mathcal{S} \subset \mathbb{R}^l$ the predicted outcome from the ANN, where $\mathbf{u}$ denotes the deterministic inputs of the ANN like the number of layers and neurons per layer, the activation functions in each of the hidden and output layers, along with the weights of the neurons. In our approach, $f(\cdot)$ represents the ANN-based forward model for LW prediction based on the input, yet uncertain, damage parameters $\boldsymbol{\theta}$, and $\widehat{s}$ represents the ANN-predicted ultrasonic signal response. The initial uncertainty about $\boldsymbol{\theta}$ is expressed by the *prior* PDF, which quantifies our initial degree of belief about the plausibility of the damage parameter values. By Bayes' theorem, the prior PDF can be updated using the information in the dataset $\mathcal{D}$, as follows:

$$p(\boldsymbol{\theta}|\mathcal{D}) = \frac{p(\mathcal{D}|\boldsymbol{\theta})p(\boldsymbol{\theta})}{\int_{\boldsymbol{\Theta}} p(\mathcal{D}|\boldsymbol{\theta})p(\boldsymbol{\theta})d\boldsymbol{\theta}} \tag{1}$$

where $p(\boldsymbol{\theta}|\mathcal{D})$ is the *posterior* PDF of the model parameters given the data, and $p(\mathcal{D}|\boldsymbol{\theta})$ is known as the *likelihood function*. This function measures how likely the model specified by the parameters $\boldsymbol{\theta}$ reproduces the observed data $\mathcal{D}$. The integral in the denominator is typically difficult to evaluate, however it is circumvented through stochastic simulation [38]. In complex and practical applications, the likelihood function is

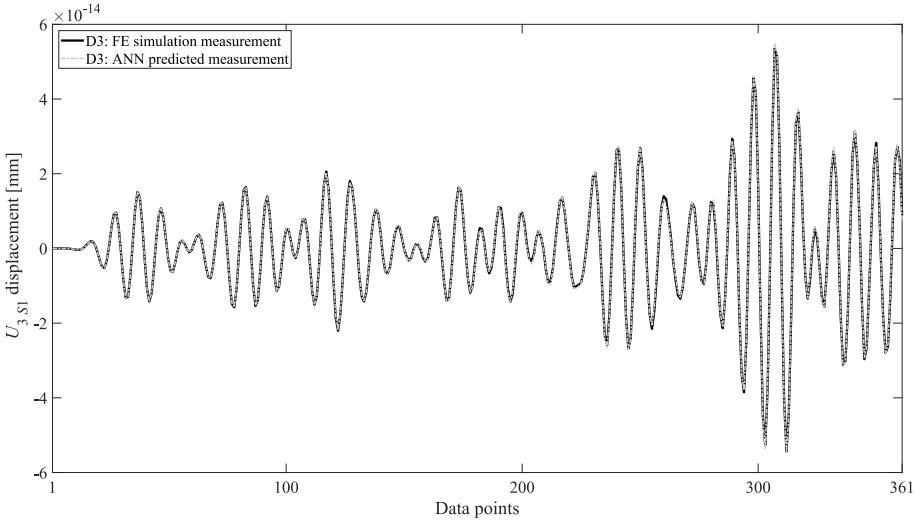

Fig. 6. A sample result of the ANN prediction of LW sensor measurement compared to the signal obtained using FE simulation, both obtained for the damage case D3.

unknown or analytically intractable, for which Approximate Bayesian Computation (ABC) methods [39] provide an efficient alternative at the cost of producing the posterior PDF $p(\boldsymbol{\theta}|\mathcal{D})$ under a tolerance error $\varepsilon \in \mathbb{R}$, namely $p_\varepsilon(\boldsymbol{\theta}|\mathcal{D})$. This precisely happens when inferring uncertain parameters from an ANN-based model, since the likelihood function of an ANN is unknown unless unjustifiably adopting a predefined probabilistic model (e.g., a Gaussian) for it. Indeed, through a tolerance parameter ε, the ABC method can produce posterior samples of the pairs $(\boldsymbol{\theta}, \widehat{s}) \in \boldsymbol{\Theta} \times \mathcal{S}$ without the need of a formal likelihood function, which makes the model response $\widehat{s} = f(\boldsymbol{\theta}, \mathbf{u}) \sim p(\widehat{s}|\boldsymbol{\theta})p(\boldsymbol{\theta})$ lay within a defined region around the data $s \in \mathcal{D}$. This region can be formally defined as:

$$\mathcal{N}_\varepsilon(s) = \{\widehat{s} \in \mathcal{S} : \rho(\zeta(\widehat{s}), \zeta(s)) \leqslant \varepsilon\} \tag{2}$$

where $\rho(\cdot) : \mathbb{R}^l \to \mathbb{R}$ is a comparison distance metric between the ANN-predicted model output $\widehat{s}$ and the data s, and $\zeta(\cdot)$ is a summary statistic which, if required, allows this comparison in a weak manner [40]. The aforementioned posterior samples produce an approximation of the posterior PDF $p_\varepsilon(\boldsymbol{\theta}, \widehat{s}|s) = p(\boldsymbol{\theta}, \widehat{s}|\widehat{s} \in \mathcal{N}_\varepsilon(s))$, which by Bayes' theorem can be written as:

$$p_\varepsilon(\boldsymbol{\theta}, \widehat{s}|\mathcal{D}) \propto P(\widehat{s} \in \mathcal{N}_\varepsilon(s)|\boldsymbol{\theta}) p(\widehat{s}|\boldsymbol{\theta}) p(\boldsymbol{\theta}) \tag{3}$$

In the last equation $P(\widehat{s} \in \mathcal{N}_\varepsilon(s)|\boldsymbol{\theta})$ is the approximated likelihood function which is evaluated through simulation adopting the unity when $\rho(\zeta(\widehat{s}), \zeta(s)) \leqslant \varepsilon$, and 0 otherwise. Also, $P(\cdot)$ denotes probability whilst $p(\cdot)$ refers to a PDF. Since ultimate interest relies on the approximate posterior of the model parameters, this can be straightforwardly obtained as:

$$p_\varepsilon(\boldsymbol{\theta}|\mathcal{D}) \propto P(\widehat{s} \in \mathcal{N}_\varepsilon(s)|\boldsymbol{\theta}) p(\boldsymbol{\theta}) \tag{4}$$

4.1. ABC-SubSim for damage inference using one sensor measurement

In ABC, the choice of ε is a matter of the amount of computational effort that the user wishes to expend. For a sufficiently small value ($\varepsilon \to 0$), then $\widehat{s} \to s$, and all accepted samples come from the closest approximation to the required posterior. This desirable fact is at the expense of a high computational effort (usually prohibitive) to get $\widehat{s} = s$ using the forward model, i.e., using the ANN surrogate model in this case. On the contrary, as $\varepsilon \to \infty$, all accepted observations come from the prior. Therefore, the choice of an adequate and sufficiently small ε reflects a trade-off between computability and accuracy. Thus, the ABC-SubSim merges the ABC principle with the technique of *Subset Simulation* [41] to achieve computational efficiency for very small ε values. It was proposed by Chiachío et al. [22] as a combination between the ABC algorithm and a highly efficient rare-event sampler that draws conditional samples from a nested sequence of simulation levels, also referred to as *subsets*. Fig. 7 provides a simplified flowchart explaining the implementation of ABC-SubSim for LW-based damage inference using one sensor measurement. The algorithm is implemented such that a maximum number of simulation levels m is allowed in case the specified final tolerance parameter ε_f is too small. The algorithm starts by generating N samples of random damage parameters that satisfy the problem's geometric conditions, which are described through the prior PDF of the damage parameters. Each random sample is denoted by $\widetilde{\boldsymbol{\theta}}$, and feeds the ANN-based surrogate LW model to generate a predicted sensor measurement $\widehat{s} = f(\widetilde{\boldsymbol{\theta}}, \mathbf{u})$. The resulting N distances $\rho(\cdot)$ between the predicted sensor measurements and the actual sensor measurement s are then calculated, whereby the sampled parameters $\widetilde{\boldsymbol{\theta}}$ can be sorted. A selection of Np_0 samples from the lowest $\rho(\cdot)$ values are chosen out of the N available samples, where $p_0 \in \mathbb{R}$ is a user-defined conditional probability value [41,42]. The chosen samples are used as seeds to generate more samples closer to s, until a set of N samples is reached. This finalizes one simulation level, where new N samples, closer to s, are available for the next simulation level. The tolerance parameter ε, attained at the current simulation level, is obtained as the average between the Np_0^{th} and the $(Np_0+1)^{th}$ set of ρ distances. If the stopping criterion $\varepsilon \leq \varepsilon_f$ is satisfied, the algorithm stops, otherwise, this process is repeated up to m simulation levels, where m can be fixed after a trial and error process. For sample generation, the chosen Np_0 samples are used as seeds for Np_0 Markov chains of length $1/p_0$ each, where the new $(1/p_0 - 1)$ samples in each chain are generated by the modified Metropolis algorithm (MMA) [41,42]. Note that each one of the seeds is used as a "parent" from which $(1/p_0 - 1)$ "children" samples are generated sequentially. In this case, the predicted sensor measurement $\widehat{s}$ of each newly generated child is tested against the real sensor measurement s through the distance metric. If the distance between s and $\widehat{s}$ is less than or equal to the current tolerance parameter ($\rho \leq \varepsilon$), then the child is accepted, otherwise, the child is replaced by its previous parent sample. This sample generation process shows the strength that *Subset Simulation* adds to ABC, given that a small probability is converted into a sequence of larger conditional probabilities. A new generation of samples is bred out of the best samples from the previous generation, where accepting new samples depends on their evaluation based on the proposed

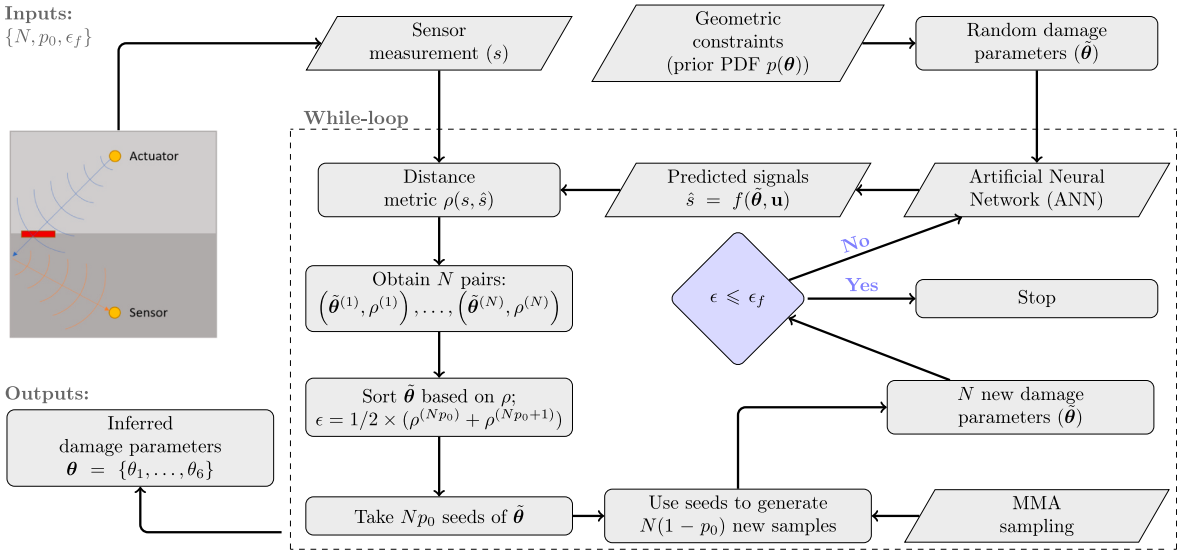

Fig. 7. A flowchart explaining ABC-SubSim damage inference within the context of damage parameter inference from one LW sensor measurement using an ANN Lamb-wave surrogate model.

distance metric ρ. Repeating this process over several simulation levels leads to the convergence into a rich *approximated posterior*, while attaining a low enough tolerance parameter ε_f. Finally, regarding the distance metric, the well known *cosine* distance was chosen as a metric for comparison between the real s and the ANN-predicted $\widehat{s}$ ultrasonic signals. The metric was modified to have a range of $0 \leq \rho \leq 1$, as shown next in Equation (5):

$$\rho(s,\widehat{s}) = 1 - \left| \frac{\widehat{s}s'}{\sqrt{(\widehat{s}\widehat{s}')(ss')}} \right| \tag{5}$$

where $\widehat{s}'$ and s' are, respectively, the transposes of the signals $\widehat{s}$ and s, treated as vectors of data points.

4.2. Data fusion: applying ABC-SubSim to multiple sensor measurements

To obtain an accurate and robust damage inference, more than one sensor measurement may be used. The application of ABC-SubSim using multiple sensor measurements requires the use of multiple LW surrogate models each for the prediction of one of the sensor measurements, as mentioned earlier in Section 3.1. Thus, assuming the use of M sensing points, the set $\{s_1, \ldots, s_M\}$ of reference signals are obtained. Similarly, a number M of ANNs can be employed to predict the LW signal responses for each damage case, thus leading to a total of M predictions, namely $\{\widehat{s}_1, \ldots, \widehat{s}_M\}$. Both sets are then compared using data fusion of the M sensing points whereby the distances are all merged into one overall distance metric ρ_T, as follows:

$$\rho_T = \prod_{j=1}^{M} \rho(\widehat{s}_j, s_j) \tag{6}$$

where j is the index of the corresponding sensor measurement, ranging from 1 to M. Note that the combined metric from the previous equation makes $\rho_T = 0$ if any individual distance $\rho(\widehat{s}_j, s_j) = 0$ for any $j = 1, \ldots, M$, hence it works equivalently to a logical AND operator. After the metric combination, each sample damage parameter $\widetilde{\boldsymbol{\theta}}$ will have a joint corresponding distance metric ρ_T, and the rest of the algorithm can then be continued similar to ABC-SubSim using a single sensor measurement, as depicted in Fig. 7.

5. Results and discussion

In this section, the results of applying the proposed method are shown for damage detection and identification, and discussion is provided about the inference evaluation along with the use of one or several sensing points. The values of ABC-SubSim control parameters that are used in this study are listed in Table 4. Finally, the prior distributions adopted for model parameters $\boldsymbol{\theta}$ are component-wise uniforms defined over the intervals given in Table 5.

5.1. Damage detection

Here the method is tested for damage detection purposes, to which the inference of an intact weld using U_{2S1} is analyzed. To ensure that the healthy case can still be captured in the presence of noise, the intact signal is corrupted with random colored noise of a frequency up to 450 [kHz]. The maximum noise level is 3% of the healthy signal's maximum amplitude. For this analysis, a damage detection rule was set such that all the three damage size parameters $\{\ell, w, t\}$ should surpass their set thresholds (α, β, γ), respectively to indicate that a wormhole damage exists. Since the targeted damage type is the wormhole welding defect (a relatively macro-sized damage type), the thresholds were chosen to be $\alpha = 1$, $\beta = 0.1$, and $\gamma = 0.1$, expressed in millimeters. Note that size thresholds are problem specific and should be chosen carefully based on the problem at hand and the targeted damage types and shapes.

Table 4
ABC-SubSim algorithm hyper-parameters used in this study.

Algorithm hyper-parameter	Value	Description
N	8000	Samples/simulation level
m	$\leqslant$13	Simulation levels
ε_f	10^{-6M}	Tolerance value
p_0	0.25	Cond. Probability

Table 5
Range of definition of the prior PDFs of damage parameters, which are component-wise considered as uniforms.

Damage parameter	ℓ	w	t	x	y	z
Minimum value [mm]	0	0	0	−125	−1.5	−1.5
Maximum value [mm]	250	3.2	3	125	1.5	1.5

The inference results are visualized in Fig. 8 as scatter plots of the approximated posterior of the damage parameters $\boldsymbol{\theta} \sim p_\varepsilon(\boldsymbol{\theta}|\mathcal{D})$ determined by the ABC-SubSim algorithm. The plots on the diagonals are probability histograms representing the inferred posterior PDF of each of the damage parameters. To select a representative realization from the posterior PDF of damage parameters, the *maximum a posteriori* (MAP) of the damage parameters, referred to as $\boldsymbol{\theta}_{MAP}$, is adopted based on the posterior PDF $p_\varepsilon(\boldsymbol{\theta}|\mathcal{D})$. The results reveal MAP values for the size parameters as follows: $\ell = 25.2$, $w = 0.02 < \beta$, and $t = 0.01 < \gamma$, given in millimeters. Note that even though the length parameter has not been successfully inferred, it can still be concluded that there is no damage within the weld from the inference of the width (w) and thickness (t) damage parameters, as depicted in second and third columns in Fig. 8. Thus, the virtual position of the non-existent damage can be anywhere as predicted in the scatter plots of the position parameters, given in the last three columns of the referred figure.

5.2. Damage identification and inference evaluation using one sensor measurement

This section presents the results of the damage parameter inference in the weld joint taken as a case study. Since many testing damage cases are available (namely 594 cases), only 18 representative cases are chosen to be analyzed and discussed. Table 6 lists the nominal damage parameters of the chosen damage cases whereby the simulated ultrasound signals were produced. To reproduce a more realistic sensor measurement, the FE data of each testing damage case were contaminated with random colored noise, as was done previously with the intact signals. In addition to noise contamination, it is important to remark that the damage cases used for testing the suggested framework were not included within the training dataset of the ANN surrogate models. Additional discussions and results of higher noise contamination levels can be viewed in Section 6 and Tables 12 and 13 in Appendix B. Figs. 9 and 10 show the ABC-SubSim damage inference results of two test cases using U_{3S1}. Fig. 9 shows the scatter plots of the inferred $\boldsymbol{\theta}$ values for the test case 15, starting from the prior at the first simulation level and until reaching the approximated posterior at the final simulation level, which in this case corresponds to $m = 13$, and is marked in blue color. Samples of the intermediate simulation levels are drawn using increasing gray tones to show the algorithm's convergence towards the final damage inference. The empty and less dense regions in the prior reveal the geometric constraints that were imposed by the problem at hand. The red dotted lines indicate the actual values of the damage. Fig. 10 displays the final approximated posterior of another test case, namely the test case 5, along with the labels of the true damage parameters. The results show that the damage parameters are still efficiently inferred using only one sensor measurement. However, when trying to capture a small damage of 25 [mm] length, some scatter plots appear to be more spread over the damage parameter ranges. Although the highest probabilities (seen on the diagonal plots) are close enough to the actual

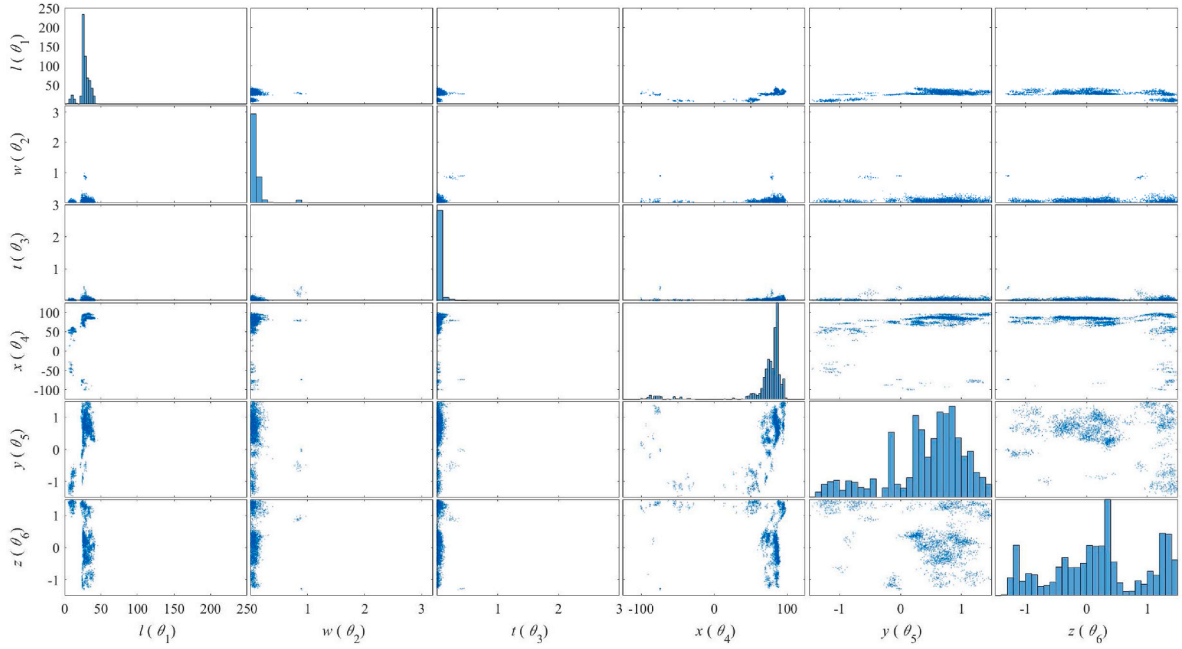

Fig. 8. ABC-SubSim damage inference results of the intact weld using U_{2S1} and $m = 11$ simulation levels. Units are expressed in [mm].

Table 6
Values of the parameters of the selected damage cases for inference. Units are expressed in [mm].

Case	ℓ	w	t	x	y	z	$\boldsymbol{\theta}$
1	25	1	1	−75	−1	−1	[25, 1, 1, − 75, − 1, − 1]
2	25	1	2	0	1	0	[25, 1, 2, 0, 1, 0]
3	25	2	1	−50	0	−0.5	[25, 2, 1, − 50, 0, − 0.5]
4	25	2	2	50	−1	−0.5	[25, 2, 2, 50, − 1, − 0.5]
5	25	3	1	0	0	0	[25, 3, 1, 0, 0, 0]
6	25	3	2	50	1	−0.5	[25, 3, 2, 50, 1, − 0.5]
7	100	1	1	−75	−1	−1	[100, 1, 1, − 75, − 1, − 1]
8	100	1	2	0	1	0	[100, 1, 2, 0, 1, 0]
9	100	2	1	−50	0	−0.5	[100, 2, 1, − 50, 0, − 0.5]
10	100	2	2	50	−1	−0.5	[100, 2, 2, 50, − 1, − 0.5]
11	100	3	1	0	0	0	[100, 3, 1, 0, 0, 0]
12	100	3	2	50	1	−0.5	[100, 3, 2, 50, 1, − 0.5]
13	200	1	1	0	−1	−1	[200, 1, 1, 0, − 1, − 1]
14	200	1	2	0	1	0	[200, 1, 2, 0, 1, 0]
15	200	2	1	0	0	−0.5	[200, 2, 1, 0, 0, − 0.5]
16	200	2	2	0	−1	−0.5	[200, 2, 2, 0, − 1, − 0.5]
17	200	3	1	0	0	0	[200, 3, 1, 0, 0, 0]
18	200	3	2	0	1	−0.5	[200, 3, 2, 0, 1, − 0.5]

values for all the damage parameters, the higher spreads in some scatter plots reveal that the inference is subject to higher uncertainty. Hence, a quantitative approach is used to evaluate the quality of the damage inference in terms of uncertainty and precision, thus making the damage inference results more comparable and physically meaningful.

To this end, the precision of the damage inference, denoted by η (in %), is evaluated through the MAP value using the following expression:

$$\eta(\%) = 100 \cdot \left(1 - \frac{|\theta - \theta_{MAP}|}{\theta_{\max} - \theta_{\min}}\right) \tag{7}$$

where $\theta_{\max}$ and $\theta_{\min}$ are the set of maximum and minimum allowed values of the damage parameter $\theta \in \Theta$, respectively, as specified in Table 5. Note that Equation (7) gives an array of six precision values, each corresponding to one component-wise damage parameter θ_1, …, θ_6. Here, a value of 90% is adopted as acceptable precision threshold, which means that the error in predicting the damage parameter is 10% of the damage parameter's range, imposed by the problem's geometrical constraints. On the other hand, the uncertainty in the damage inference, as a measure of how unconfident the inference is and referred to here as ξ, is accounted for through the following expression:

$$\xi(\%) = 100 \cdot \frac{2 \cdot \mathrm{std}(\theta)}{\theta_{max} - \theta_{min}} \tag{8}$$

where std(θ) is the standard deviation of the approximated posterior PDF of parameter $\theta \in \Theta$. In this work, a 15% uncertainty threshold is adopted for inference evaluation. Tables 10 and 11 given in Appendix A present a summary of inference evaluation of the 18 chosen testing damage cases using U_{2S1} and U_{3S1}, respectively. Damage parameters that are inferred with a precision of less than 90% or with an uncertainty above 15%, are marked in red color. The values in the tables written in bold are not to be considered at this level due to a symmetry effect related to $S1$, which will be discussed further below in detail. The results from the aforementioned tables reveal high uncertainty in the inference of at least one of the damage parameters for 9 out of the 18 damage cases when using the measurement U_{2S1}, and for 11 out of the 18 damages cases when using the measurement U_{3S1}. Note that higher uncertainties and lower precision in the damage prediction are mostly associated with the first six damage cases, where the damage length is relatively small ($\ell = 25$ [mm]). Additionally observe that the damage cases of noticeable damage, i.e., $\ell = 200$ [mm] (test cases 13 to 18) are better inferred, with high precision and low uncertainties for both sensor measurements. Finally note that damage cases of $\ell = 100$ [mm] (test cases 7 to 12) are inferred with high precision as well, however, more uncertainties exist among their results.

Besides, Fig. 11 shows ABC-SubSim damage inference results of the test case 12 using U_{2S1}. Observe that while all damage parameters are well inferred, two x-positions of opposite values are obtained. This is due to the symmetry associated with the sensing point $S1$, as both the actuator and $S1$ are located within the YZ-plane, the plane of symmetry of the plate. This is illustrated in Fig. 12a on an example of two identical damages, each having an opposite x-position with respect to the other. The two damages are symmetric with respect to the YZ-plane, where both the actuator and the sensor are located. Hence, since there is no noise, nor variation in the boundary conditions, neither any other factor affecting the measurements, the two damage cases yield the same LW measurements at the sensor. This fact should be taken into consideration

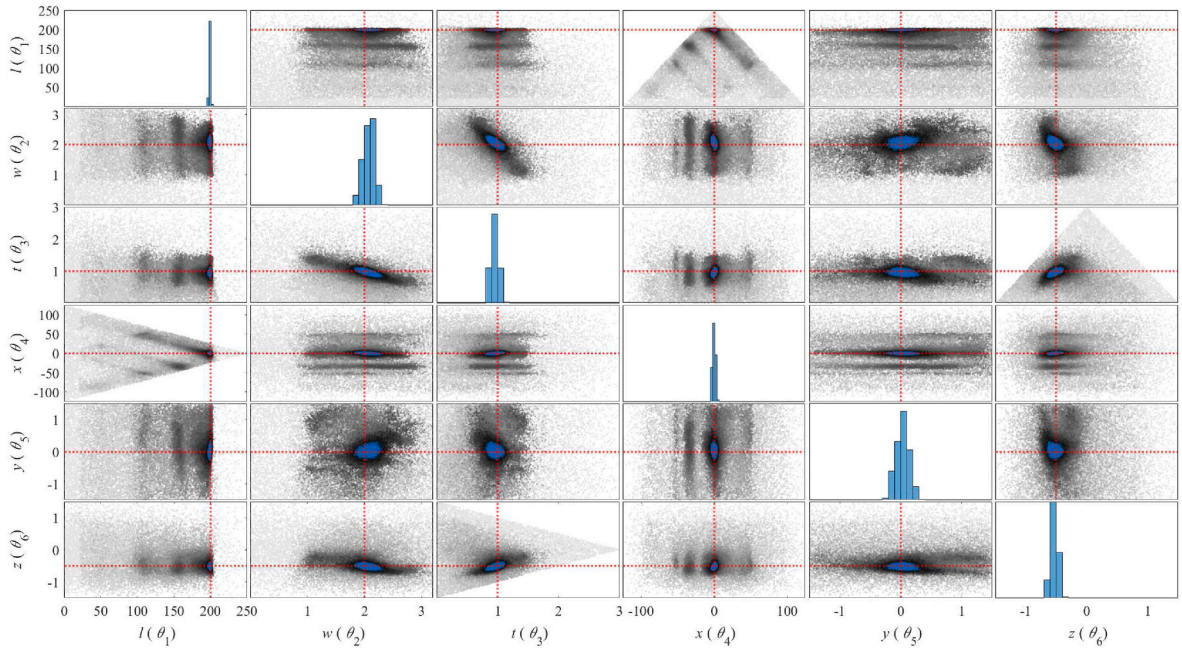

Fig. 9. Scatter plot representation of samples of the $\boldsymbol{\theta}$ space at different simulation levels as output of the ABC-SubSim algorithm applied to test case 15 (refer to Table 6) using U_{3S1} and $m = 13$ simulation levels. The final *posterior* samples are marked in blue. To reveal the uncertainty reduction, the intermediate posterior samples are superposed in increasing gray tones. On the diagonal, histogram estimates are drawn for the marginal posterior PDFs of the respective parameters. The true damage parameters are marked using red dotted lines. Units are expressed in [mm]. (For interpretation of the references to color in this figure legend, the reader is referred to the Web version of this article.)

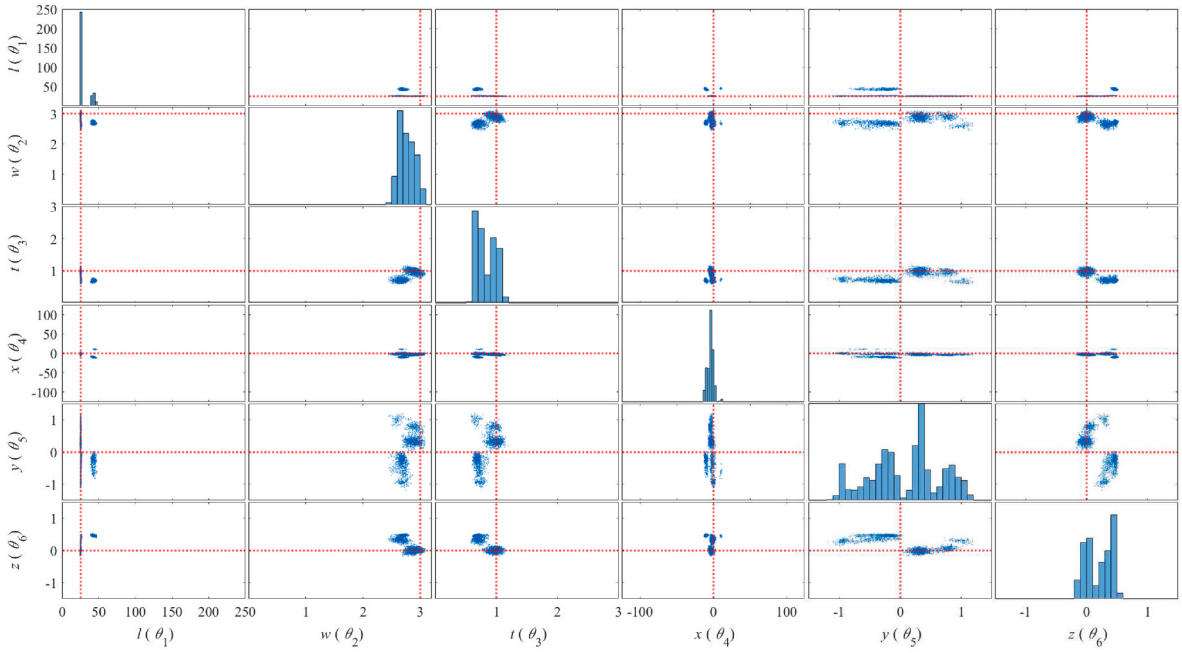

Fig. 10. ABC-SubSim damage inference results of test case 5 (refer to Table 6) using U_{3S1}, and $m = 12$ simulation levels. The true damage parameters are marked using red dotted lines. (For interpretation of the references to color in this figure legend, the reader is referred to the Web version of this article.)

when trying to infer the damage parameters using measurements from a single sensing point ($S1$). To verify this concept, U_{2S1} simulation results of the damage case D2 were compared to those of the damage case having the same damage parameters but an opposite x-position; i.e., D2-sym: $\{\ell = 50, w = 2, t = 1.5, x = 75, y = 0, z = 0.25\}$, expressed in millimeter units. The results show that the two signals overlap without any visible difference, as depicted in Fig. 12b. Moreover, it is evident in Tables 10 and 11 that either of the symmetric x-positions is successfully inferred in all of the test cases (values written in bold). The other symmetric values are also predicted but with a lower probability. This can be seen when visualizing the approximated posterior PDF of model parameters $\boldsymbol{\theta}$, as was shown in Fig. 11.

5.3. Inference results based on multiple sensor measurements

To avoid the symmetry effect described in the previous section, two

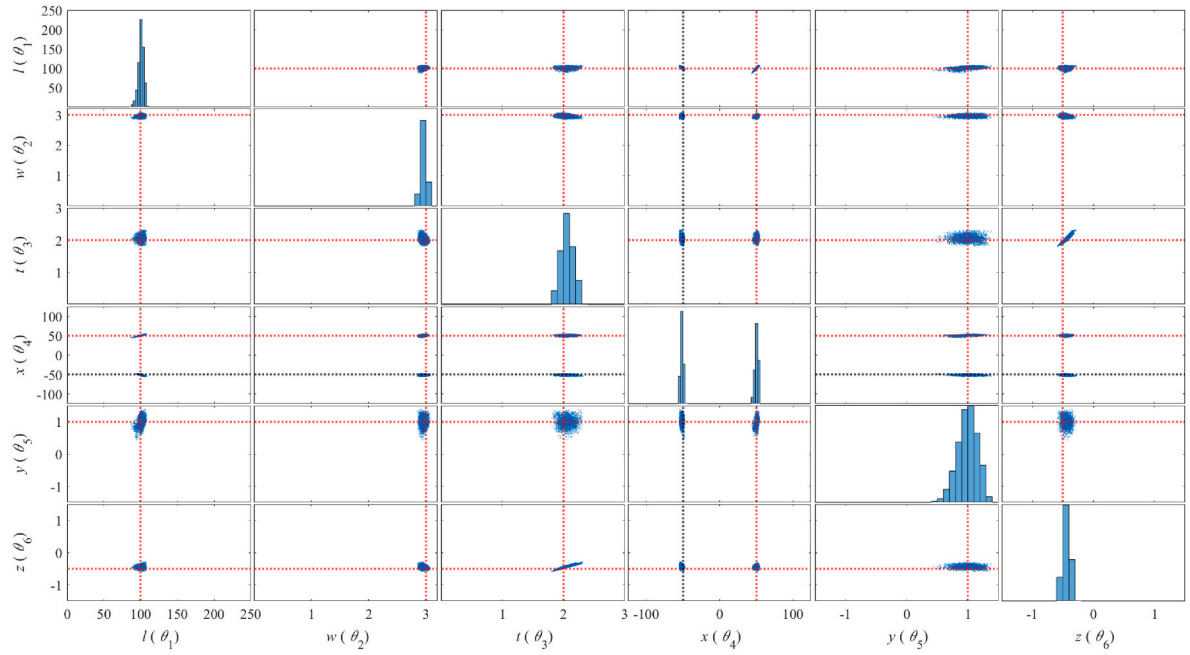

Fig. 11. ABC-SubSim damage inference results of test case 12 (refer to Table 6) using U_{2S1}, and $m = 13$ simulation levels. The true damage parameters are marked using red dotted lines. (For interpretation of the references to color in this figure legend, the reader is referred to the Web version of this article.)

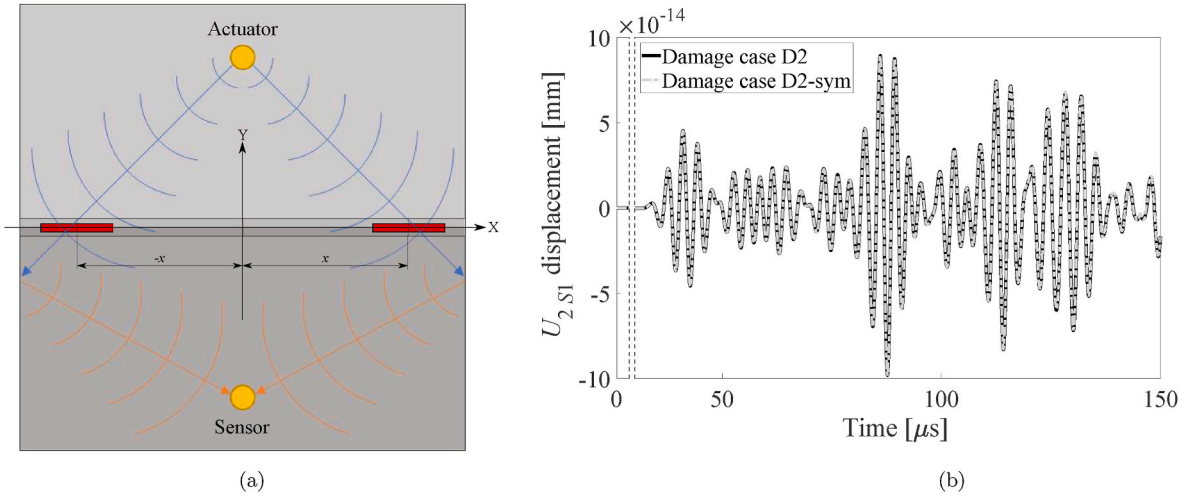

Fig. 12. Panel (a): illustration demonstrating the need for using the whole signal, including the wave's boundary reflections, to perceive damages lying outside the coverage of the sensing path. The illustration also shows how two symmetric damage cases would yield the same LW measurement at a sensor located along the $Y-$ axis. The damages are drawn in red color. Panel (b): FE results of symmetric sample damage cases; D2: $\ell = 50$, $w = 2$, $t = 1.5$, $x = -75$, $y = 0$, $z = 0.25$; D2-sym: $\ell = 50$, $w = 2$, $t = 1.5$, $x = 75$, $y = 0$, $z = 0.25$; all units are expressed in [mm]. (For interpretation of the references to color in this figure legend, the reader is referred to the Web version of this article.)

additional sensing points are used as shown in Fig. 13. The coordinates of the two added sensing points, with respect to the coordinate axis defined at the center of the plate, are $S2(-100, -80)$ and $S3(-100, 80)$, expressed in [mm]. Similar to $S1$, displacements in the U_2 and U_3 directions were recorded, and the same methodology was repeated for all the sensor measurements (U_{2S2}, U_{3S2}, U_{2S3}, and U_{3S3}), including pre-processing, data balancing, sample reduction, ANN training, and ABC-SubSim damage inference. Fig. 14 shows the boxplots summarizing ABC-SubSim damage inference results for the whole testing dataset (594 cases) using U_{2S2}. Results of different damage lengths are separated to investigate the effect of the damage size on the accuracy of prediction. The boxplot of each damage parameter consists of a box bounded by the 25th and 75th percentiles (lower and upper quartiles) of the 594 inferences, with a central mark representing the median. Hence, the interquartile range (IQR) represented within the box signifies 50% of the plotted inference cases. The whiskers extend from the box edges up to a maximum length of 1.5 × IQR, such that points lying outside this range are considered outliers and are plotted separately. Specially note that very narrow IQRs are observed in this case for the inference of the x-position, showing high precision (above 98%) and low uncertainty (below 4%). Indeed, few outliers lie within regions of precision below 90% or uncertainty above 15%. This confirms the resolution of the symmetry problem when using extra sensing points outside the plane of symmetry. Note also that moving the actuator to a position outside the plane of symmetry would have also solved the problem. Moreover, note that the damage length (ℓ) is accurately identified as well in all the testing dataset with few outlier cases, as depicted in Fig. 14. Finally, note as well that wider IQRs and more outliers are observed for the inference

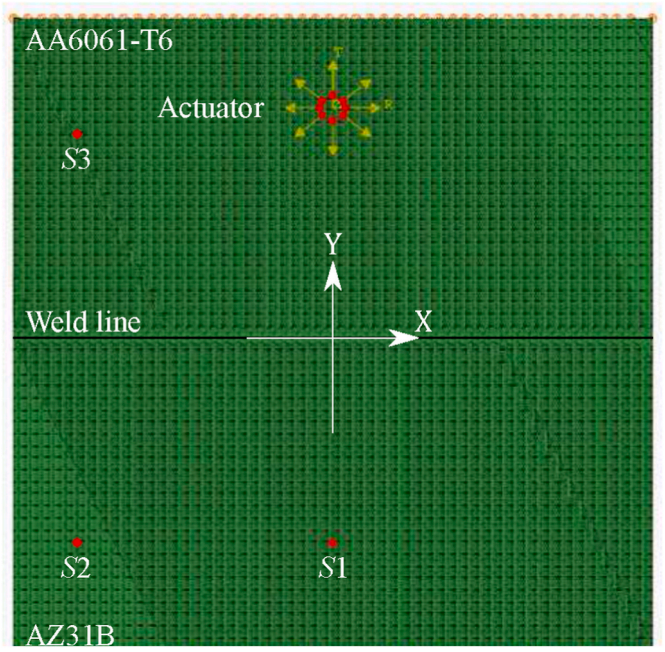

Fig. 13. The FE model showing the two added sensing points $S2$ and $S3$ (in red). (For interpretation of the references to color in this figure legend, the reader is referred to the Web version of this article.)

of damages of small extent, with $\ell = 25$ [mm] (Fig. 14a). Particularly, the damage width (w) and y-positions in those cases are inferred with higher percentages within the unacceptable thresholds of precision (<90%) and uncertainty (>15%). Contrarily, note that higher precisions and lower uncertainties are generally attained for $\ell = 100$ [mm] (Fig. 14b), and very accurate predictions are achieved in the case of $\ell = 200$ [mm] (Fig. 14c).

5.4. Inference results using data fusion

To further overcome the shortages of using a single sensor measurement along with to improve the robustness and accuracy of the inference results for inference of small damages, data fusion from two or more sensing points was performed. To this end, combinations of U_2 measurements from different sensing points were used together by employing the methodology explained in Section 4.2. Table 7 summarizes the inference results of test cases 1 to 6 ($\ell = 25$ [mm]) when using U_{2S1} and U_{2S2} together, while Table 8 summarizes those of fusing U_{2S2} with U_{2S3}. Finally, Table 9 provides the results of fusing U_2 measurements from all the three sensing points $S1$, $S2$, and $S3$. In general, the results show that both damage length ℓ and x-position are inferred with a precision higher than 99% for all the shown cases and combinations of sensing points. Very low uncertainties are also attained for both damage parameters. This proves the high potential of the data fusion technique for accurately assessing these two important parameters defining the length of the wormhole and its position along the weld. The best inference results are obtained when merging U_2 measurements from $S2$ and

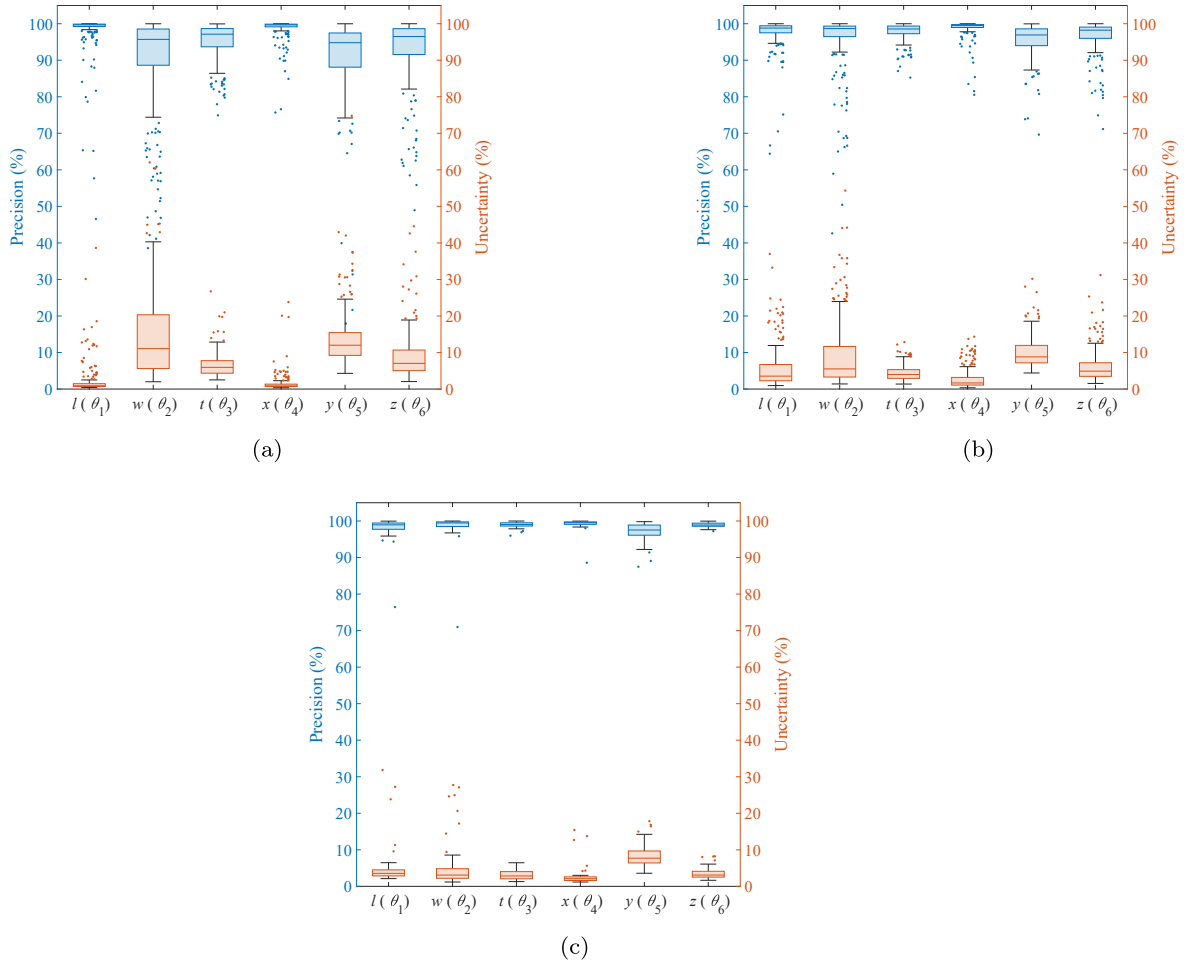

Fig. 14. Boxplots summarizing the precision and uncertainty of ABC-SubSim damage inference for the whole testing dataset (594 cases) using U_{2S2}. Results of different damage lengths are shown separately for (a): $\ell = 25$ [mm]; (b): $\ell = 100$ [mm]; and (c): $\ell = 200$ [mm].

Table 7
A summary of the ABC − SubSim inference results using U_{2S1} and U_{2S2} sensor measurements, for the testing damage cases 1 to 6.

Case	$\boldsymbol{\theta}$ [mm]	$\boldsymbol{\theta}_{MAP}$[mm]	η (%)	ξ (%)
1	[25, 1, 1, −75, −1, −1]	[25.26, 1.74, 1.10, −74.78, −0.89, −0.64]	[99.90, 76.97, 96.56, 99.91, 96.49, 87.87]	[0.36, 17.57, 7.43, 0.64, 16.63, 11.11]
2	[25, 1, 2, 0, 1, 0]	[24.93, 0.96, 2.06, 1.26, 0.17, 0.01]	[99.97, 98.62, 98.09, 99.49, 72.29, 99.69]	[0.22, 5.86, 9.12, 2.02, 14.84, 5.94]
3	[25, 2, 1, −50, 0, −0.5]	[25.40, 2.06, 1.00, −50.15, −0.25, −0.58]	[99.84, 98.05, 99.97, 99.94, 91.82, 97.42]	[0.42, 9.59, 6.21, 0.93, 10.55, 9.71]
4	[25, 2, 2, 50, −1, −0.5]	[25.07, 2.45, 1.85, 50.78, −0.86, −0.47]	[99.97, 86.05, 95.08, 99.69, 95.28, 98.91]	[0.24, 33.85, 9.09, 1.05, 9.73, 9.17]
5	[25, 3, 1, 0, 0, 0]	[25.33, 2.96, 0.96, 1.90, 1.31, −0.01]	[99.87, 98.86, 98.83, 99.24, 56.43, 99.61]	[5.55, 2.11, 8.21, 3.57, 40.63, 5.42]
6	[25, 3, 2, 50, 1, −0.5]	[25.07, 2.82, 1.93, 48.42, 0.54, −0.19]	[99.97, 94.48, 97.71, 99.37, 84.83, 89.62]	[0.26, 9.18, 4.96, 0.97, 14.58, 8.95]

Table 8
A summary of the ABC-SubSim inference results using U_{2S2} and U_{2S3} sensor measurements, for the testing damage cases 1 to 6.

Case	$\boldsymbol{\theta}$ [mm]	$\boldsymbol{\theta}_{MAP}$ [mm]	η (%)	ξ (%)
1	[25, 1, 1, −75, −1, −1]	[24.34, 0.97, 0.98, −75.74, −1.07, −0.94]	[99.74, 99.12, 99.48, 99.70, 97.63, 98.15]	[0.75, 19.77, 6.30, 0.66, 7.50, 4.48]
2	[25, 1, 2, 0, 1, 0]	[25.11, 0.93, 2.10, −0.15, 0.75, −0.11]	[99.96, 97.86, 96.55, 99.94, 91.57, 96.30]	[1.18, 8.62, 10.04, 0.85, 9.86, 11.13]
3	[25, 2, 1, −50, 0, −0.5]	[25.19, 2.10, 0.99, −50.24, 0.00, −0.56]	[99.92, 96.81, 99.77, 99.90, 99.94, 98.15]	[0.48, 7.51, 4.89, 0.67, 7.14, 8.57]
4	[25, 2, 2, 50, −1, −0.5]	[26.80, 1.12, 2.23, 51.07, −0.74, −0.32]	[99.28, 72.55, 92.26, 99.57, 91.30, 94.06]	[0.72, 26.47, 11.32, 0.78, 12.93, 6.10]
5	[25, 3, 1, 0, 0, 0]	[23.72, 3.02, 1.10, −0.22, 0.26, −0.09]	[99.49, 99.35, 96.61, 99.91, 91.42, 97.11]	[0.97, 3.25, 8.56, 0.82, 14.62, 5.97]
6	[25, 3, 2, 50, 1, −0.5]	[25.11, 2.90, 2.13, 48.61, 1.00, −0.37]	[99.96, 96.82, 95.53, 99.45, 100.0, 95.65]	[0.45, 10.95, 8.58, 0.91, 10.10, 7.13]

Table 9
A summary of the ABC − SubSim inference results using the three sensor measurements (U_{2S1}, U_{2S2}, and U_{2S3}), for the testing damage cases 1 to 6.

Case	$\boldsymbol{\theta}$ [mm]	$\boldsymbol{\theta}_{MAP}$ [mm]	η (%)	ξ (%)
1	[25, 1, 1, −75, −1, −1]	[25.11, 1.15, 1.00, −74.83, −0.74, −0.93]	[99.96, 95.17, 99.84, 99.93, 91.41, 97.62]	[0.34, 22.89, 6.72, 0.56, 11.31, 5.03]
2	[25, 1, 2, 0, 1, 0]	[25.18, 0.89, 1.85, 1.13, 0.44, −0.01]	[99.93, 96.53, 95.12, 99.55, 81.21, 99.54]	[0.30, 5.39, 6.07, 1.13, 15.27, 6.48]
3	[25, 2, 1, −50, 0, −0.5]	[25.09, 1.96, 1.00, −50.16, 0.10, −0.39]	[99.96, 98.83, 99.92, 99.93, 96.77, 96.31]	[0.42, 7.37, 6.08, 0.79, 7.73, 8.23]
4	[25, 2, 2, 50, −1, −0.5]	[25.06, 2.01, 1.91, 49.74, −1.09, −0.48]	[99.98, 99.57, 97.11, 99.89, 97.00, 99.40]	[0.27, 31.07, 10.38, 1.04, 6.69, 9.73]
5	[25, 3, 1, 0, 0, 0]	[25.60, 2.97, 1.08, 1.15, 0.16, −0.11]	[99.76, 99.08, 97.20, 99.54, 94.64, 96.48]	[0.56, 2.42, 10.08, 1.18, 30.07, 7.25]
6	[25, 3, 2, 50, 1, −0.5]	[25.14, 2.53, 1.95, 49.71, 0.96, −0.28]	[99.94, 85.18, 98.32, 99.89, 98.53, 92.74]	[0.27, 11.63, 6.85, 0.81, 8.64, 7.97]

$S3$, as revealed in Table 8. In this case, damage parameters are inferred with a precision of above 95% for more than 83% of the cases. Indeed, the only inference with a precision below 91% is for the damage width (w) in test case 4, with an error less 0.9 [mm]. Moreover, only two uncertainty values above the 15% threshold are recorded, which precisely also correspond for the damage width parameter (w).

The results also show that combining U_2 measurements from $S1$ and $S2$ does not produce a significant improvement with respect to the inference using one sensor measurement, as manifested in Table 7, however, combining the measurements of the three sensing points have resulted in better inference, as shown in Table 9. In this latter case, damage is inferred with high precision (>90%) for all the cases except for two damage parameters (highlighted in red), with errors less than 0.6 [mm]. Moreover, more than half of the inference results are obtained with a precision above 99%, while being above 95% happens in most of the cases.

6. Discussion on methodology

The proposed approach enables probabilistic damage detection and identification in welded structures by giving PDFs of a number of damage parameters, including size and position parameters of the damage. This overcomes deterministic identification methods since the uncertainty present in the measurements, damage model, and the method itself, can be considered and quantified, and further used for decision making. The proposed methodology has been proved capable of inferring the intact state of a monitored weld along with damage cases of different size, using only one single measurement and despite it noisy condition. This resolution in inferring a precise size and position of the damage using only one single measurement, can be considered as an important achievement in the damage identification field, where the current practice typically requires numerous arrays of sensors.

When using a single sensor measurement, two x-positions were inferred revealing a geometrical symmetry for both the actuator and the

sensing point, as expected. Nevertheless, the successful prediction of both the actual x and its symmetric value, means that the ANN-based surrogate model has effectively learned this symmetry from the training data. This result is a validation of the ANN's performance and of the methodology's potential for detecting multiple possibilities of the available damage. Notwithstanding, the symmetry problem was resolved upon using measurements from an extra sensing point lying outside the plate's plane of symmetry. In such case, damage length (ℓ) and x-position were precisely predicted even for small damage sizes, while for large damages, very accurate predictions were attained for all the damage parameters. The symmetry of $S1$ is obvious in the problem under study; however, other non-trivial similarities of measurements from different damage cases may be faced in real-life situations. Hence, data fusion from multiple sensing points (at least two sensor measurements) is thought to be a necessity to avoid such issues and increase the reliability of the damage identification process. Indeed, after fusing multiple sensor measurements (U_{2S1}, U_{2S2}, and/or U_{2S3}) within the ABC-SubSim algorithm, even higher precisions and lower uncertainties were achieved for the cases of small damage size.

Besides, it is noticed in all the presented inference results that the width (w) and the y-position show higher uncertainties accompanied sometimes with less inference precision than for the rest of damage parameters. This is most obvious when looking at damages of small size ($\ell = 25$ [mm]); i.e., for test cases 1 to 6 (Table 6). This reflects an imperfect performance of the ANN surrogate model over the w and y parameters when the damage is small. A potential solution if a better inference is desired in the case of small damages, is to include an additional inference step activated only if ℓ is inferred to be below a certain threshold in the first attempt. This would include the training of an additional ANNs using specific training data of small damage lengths only to help the ANNs better learn how to differentiate the other damage parameters. ABC-SubSim parameters may also be tuned, in this case, to make the first inference faster but probably less accurate. In practice, the SHM system designer should be aware of types, shapes, and possible positions of damages, in the monitored structure, that should be considered and modeled in the finite element model for data generation. Thus, the architecture of the trained ANN should also be adapted to the new number of input variables (size, position, and probably orientation and shape parameters of the damage) and to the new signal length, as needed. More complex damage cases can be integrated by using multiple neural networks to cover different types of damage and sizes. In this case, the problem might be split into a classification stage first, identifying the damage type using machine learning classifier(s), and then into an identification stage whereby to infer the predefined damage parameters.

An additional consideration when implementing the proposed framework, is about calibration and normalization of the sensor measurements required to make the experimental data comparable to the numerical data in terms of amplitude. A deviation in the placement of the actuators and sensors is not expected to cause a major difference in the collected responses; neither might highly impact the coverage of the sensor network [9]. Also, slight misplacement of the PZT wafers may lead to small variations in the signals which are of the level of noise, however, it was demonstrated that damage inference is robust to such disparity. Non-contact sensing and actuation methods (e.g., air-coupled or laser-based transducers) would provide a better control and data normalization ability when available. Correspondingly, the FE modeling should be modified based on the used actuation and sensing methods to produce signals that are well matching with the experimental measurements. The better the match is between the FE simulations and real experimental signals, the more robust the inference is when applied to real sensor measurements, with less yielded uncertainties. The differences in a signal that may arise due to noise or environmental changes (as temperature and pressure on an airplane structure) are expected to appear as small inference deviation rather than failure in prediction, which was corroborated by adding different levels of sensing noise, and shown in Appendix B. The results show that inference precision and uncertainty are not affected by the addition of various levels of noise for big damage cases, as shown in Table 12. For small damage cases ($\ell = 25$ [mm]), the results in Table 13 indicate that the increasing noise levels slightly affect the inference quality but without significant influence in terms of detectability and damage assessment. The results for middle-sized damages of $\ell = 100$ [mm] represent an intermediate situation between the previous damage cases cited before, thus, the analysis in Appendix B is avoided for printing space purposes.

Further, a prognostics-based decision making SHM system is envisaged as desirable future work, where the structure's deterioration and remaining useful life can be predicted to make informed decisions. A more intelligent system would also add self adaptation algorithms to dynamically account for environmental changes and operational conditions, therefore, increasing both the structure's integrity and efficiency. The usage of transfer learning algorithms could be a potential solution for such adaptation [43]. Transfer learning may be also employed when moving from FE training to experimental testing to compensate for the differences between numerical and experimental signals.

Finally, time is a key factor when monitoring critical structures that, in case of failure, may endanger people's lives. This factor is more important when such structures are subject to highly variable loads (e.g., an operating passenger airplane) or may be exposed to abrupt changes (e.g., severe impact damage). A successful SHM system should be able to detect any damage at the moment it happens or even has the potential for capturing the deterioration in the structure's strength before damage occurs. The time elapsed to perform one FE simulation was, on average, around 4.75 min using an Intel® Core™ i7-8750H CPU (parallel Abaqus® simulation over 8 CPUs). However, the ANN takes around 8 [ms] to predict the signal using the same processor. This obvious advantage (more than 35,000 times faster) and the possibility to do the ANN prediction with minimal processing needs, both give the surrogate modeling its importance for applying a probabilistic damage inference methodology in a real SHM system. The latter opens a door for the development of smart sensors for monitoring of welded structures, that include microprocessors on-board the monitored system which can detect and identify damage in real time.

7. Concluding remarks

This paper proposed a novel framework for damage detection, localization, and assessment using ultrasonic measurements. The framework allows for full identification, in size and position, of damage within a dissimilar material joint using only one ultrasonic actuator and one sensor measurement.

Surrogate models, based on *Artificial Neural Networks* (ANNs), were trained using finite element simulations to predict Lamb-wave sensor measurements when given specific damage. The ANNs were then employed to perform a probabilistic damage inference on simulated data corrupted with noise using *Approximate Bayesian Computation*, thus, providing *posterior* PDFs of six damage parameters (length, width, thickness, and x, y, and z-positions).

The potential of the algorithm for detecting multiple damage scenarios that may lead to the same sensor measurement, was proved. This made it advisable to fuse information from at least two sensor measurements to guarantee a more reliable damage identification. Upon data fusion of multiple sensor measurements, the length and x-position of the damage were inferred with a precision higher than 99% in all the test cases. The inference of the other four damage parameters (width, thickness, and y and z-positions) was attained with an error of less than 0.9 [mm], in the worst case scenario. Damage parameters were inferred with a precision of above 95% for more than 83% of the cases when using a combination of two sensor measurements (U_2 from $S2$ and $S3$).

The developed framework is computationally inexpensive, thus rendering the methodology suitable for online/onboard monitoring

applications. The high resolution attained, inferring an accurate size and position of the damage by employing only one or two sensor measurements, is considered a major advancement in the structural assessment field. Improvements and future work may include the consideration of variable environmental and operational conditions, and the incorporation of lifetime prediction and prognostics.

Credit author statement

Mohammad Ali Fakih: Investigation, Software, Formal Analysis, Writing- Original draft preparation. **Manuel Chiachío**: Conceptualization, Methodology, Visualization, Investigation, Writing- Original draft preparation, Supervision. **Juan Chiachío**: Investigation, Methodology, Writing- Review & Editing. **Samir Mustapha**: Validation, Resources, Supervision, Funding acquisition, Writing- Review & Editing.

Declaration of competing interest

The authors declare that they have no known competing financial interests or personal relationships that could have appeared to influence the work reported in this paper.

Acknowledgment

Recognition and gratitude are addressed to the National Council for Scientific Research of Lebanon (CNRS-L) for granting the first author a doctoral fellowship number #103085. Recognition is extended to the European Commission, the American University of Beirut, and the University of Granada (UGR) for their Erasmus + mobility scholarship that was granted to the first author to conduct this work at UGR, Spain.

Appendix A

Table 10
A summary of the ABC-SubSim inference results using U_{2S1} sensor measurement, for the selected damage cases.

Case	θ [mm]	θ_{MAP} [mm]	η (%)	ξ (%)
1	[25, 1, 1, −75, −1, −1]	[25.31, 1.00, 1.40, **77.40**, 0.28, −0.32]	[99.88, 99.93, 86.52, **39.04**, 57.45, 77.36]	[15.43, 19.37, 18.27, **39.77**, 26.00, 27.83]
2	[25, 1, 2, 0, 1, 0]	[25.68, 0.89, 1.78, 6.89, −0.87, 0.17]	[99.73, 96.69, 92.77, 97.24, 37.78, 94.37]	[9.95, 3.24, 9.07, 3.36, 12.97, 6.78]
3	[25, 2, 1, −50, 0, −0.5]	[25.42, 1.90, 0.92, −**48.55**, −0.56, −0.43]	[99.83, 96.97, 97.36, **99.42**, 81.49, 97.73]	[4.13, 19.75, 9.57, **32.07**, 21.13, 23.63]
4	[25, 2, 2, 50, −1, −0.5]	[24.91, 1.79, 1.90, −**50.17**, −1.03, −0.33]	[99.96, 93.46, 96.51, **59.93**, 99.10, 94.45]	[0.36, 26.90, 10.20, **22.17**, 10.84, 11.71]
5	[25, 3, 1, 0, 0, 0]	[25.30, 3.00, 0.65, −22.47, −0.01, 0.24]	[99.88, 99.95, 88.20, 91.01, 99.57, 91.94]	[18.45, 2.79, 8.07, 13.56, 11.56, 9.41]
6	[25, 3, 2, 50, 1, −0.5]	[24.88, 2.56, 2.00, −**50.77**, 1.36, −0.38]	[99.95, 86.22, 99.90, **59.69**, 88.00, 96.10]	[0.28, 6.29, 5.02, **8.88**, 19.04, 5.45]
7	[100, 1, 1, −75, −1, −1]	[97.74, 0.89, 1.15, **76.37**, −0.78, −0.86]	[99.09, 96.61, 95.00, **39.45**, 92.72, 95.47]	[1.75, 11.33, 5.66, **35.67**, 8.20, 3.86]
8	[100, 1, 2, 0, 1, 0]	[100.53, 1.01, 1.98, −1.11, 1.01, 0.00]	[99.79, 99.58, 99.49, 99.56, 99.64, 99.84]	[2.87, 2.94, 3.71, 1.76, 7.59, 2.64]
9	[100, 2, 1, −50, 0, −0.5]	[100.35, 1.97, 0.99, **45.27**, −0.08, −0.52]	[99.86, 99.01, 99.75, **61.89**, 97.17, 99.33]	[17.61, 4.66, 6.46, **35.30**, 7.18, 6.82]
10	[100, 2, 2, 50, −1, −0.5]	[100.84, 2.0, 1.88, −**49.75**, −0.98, −0.50]	[99.66, 100.0, 96.16, **60.10**, 99.37, 99.85]	[2.38, 18.18, 6.98, **39.80**, 7.03, 3.79]
11	[100, 3, 1, 0, 0, 0]	[145.10, 2.99, 0.93, 25.01, 0.18, −0.04]	[81.96, 99.65, 97.82, 90.00, 93.91, 98.61]	[15.50, 1.17, 5.67, 15.59, 16.02, 3.37]
12	[100, 3, 2, 50, 1, −0.5]	[100.67, 2.94, 2.05, −**51.15**, 1.01, −0.45]	[99.73, 98.24, 98.47, **59.54**, 99.81, 98.28]	[2.87, 2.78, 6.79, **40.71**, 10.68, 3.68]
13	[200, 1, 1, 0, -1, -1]	[200.80, 0.93, 1.06, −2.15, −0.80, −0.95]	[99.68, 97.76, 97.97, 99.14, 93.25, 98.28]	[6.08, 14.98, 4.35, 4.33, 8.26, 3.26]
14	[200, 1, 2, 0, 1, 0]	[200.62, 0.97, 2.03, 1.61, 1.09, 0.01]	[99.75, 98.91, 98.96, 99.35, 97.01, 99.71]	[1.11, 3.89, 4.52, 4.56, 10.87, 2.97]
15	[200, 2, 1, 0, 0, −0.5]	[199.95, 2.03, 1.02, −2.27, −0.02, −0.51]	[99.98, 99.21, 99.46, 99.09, 99.34, 99.83]	[6.57, 3.34, 3.33, 5.12, 6.31, 2.29]
16	[200, 2, 2, 0, −1, −0.5]	[200.16, 2.01, 1.95, −2.46, −1.07, −0.50]	[99.94, 99.57, 98.26, 99.02, 97.66, 99.95]	[0.88, 20.94, 5.39, 2.47, 5.69, 3.08]
17	[200, 3, 1, 0, 0, 0]	[195.37, 2.98, 1.08, −5.51, 0.02, 0.05]	[98.15, 99.46, 97.44, 97.80, 99.33, 98.41]	[11.95, 1.15, 5.65, 10.59, 12.21, 2.79]
18	[200, 3, 2, 0, 1, −0.5]	[178.95, 2.98, 1.99, −8.30, 0.84, −0.48]	[91.58, 99.50, 99.62, 96.68, 94.64, 99.37]	[8.81, 2.12, 6.73, 5.63, 9.63, 3.60]

Table 11
A summary of the ABC-SubSim inference results using U_{3S1} sensor measurement, for the selected damage cases.

Case	θ [mm]	θ_{MAP} [mm]	η (%)	ξ (%)
1	[25, 1, 1, −75, −1, −1]	[24.45, 1.02, 0.99, **−74.49**, −1.18, −0.98]	[99.78, 99.33, 99.62, **99.80**, 94.02, 99.35]	[0.49, 18.55, 7.50, **44.42**, 26.56, 4.98]
2	[25, 1, 2, 0, 1, 0]	[25.36, 1.02, 1.74, 0.87, −0.46, −0.00]	[99.86, 99.52, 91.19, 99.65, 51.28, 99.90]	[0.27, 17.19, 7.60, 1.50, 14.85, 3.77]
3	[25, 2, 1, −50, 0, −0.5]	[24.47, 2.04, 0.96, **−47.68**, 0.16, −0.46]	[99.79, 98.86, 98.75, **99.07**, 94.76, 98.74]	[0.35, 19.79, 9.90, **34.16**, 27.77, 6.95]
4	[25, 2, 2, 50, −1, −0.5]	[25.21, 2.32, 2.11, **−51.13**, −0.73, −0.38]	[99.92, 89.89, 96.30, **59.55**, 90.94, 96.05]	[0.63, 25.69, 10.76, **40.97**, 16.79, 5.54]
5	[25, 3, 1, 0, 0, 0]	[25.11, 2.68, 0.69, −3.34, 0.33, 0.45]	[99.95, 90.13, 89.67, 98.66, 88.92, 85.15]	[5.92, 8.23, 10.10, 3.21, 37.63, 13.98]
6	[25, 3, 2, 50, 1, −0.5]	[24.80, 1.58, 1.82, **−49.56**, 0.93, −0.48]	[99.92, 55.60, 93.85, **60.18**, 97.56, 99.48]	[0.29, 43.67, 12.26, **39.00**, 14.32, 7.25]
7	[100, 1, 1, −75, −1, −1]	[97.07, 1.12, 0.96, **75.90**, −1.05, −1.01]	[98.83, 96.13, 98.70, **39.64**, 98.46, 99.74]	[1.10, 34.18, 6.42, **59.15**, 12.49, 4.29]
8	[100, 1, 2, 0, 1, 0]	[99.54, 1.00, 1.97, −2.29, 0.87, −0.00]	[99.82, 99.97, 98.85, 99.08, 95.75, 99.85]	[8.21, 2.19, 2.65, 4.72, 26.81, 1.81]
9	[100, 2, 1, −50, 0, −0.5]	[100.78, 1.84, 1.06, **49.99**, 0.18, −0.40]	[99.69, 94.96, 97.93, **60.00**, 94.03, 96.51]	[1.36, 6.18, 5.06, **32.21**, 9.81, 4.08]
10	[100, 2, 2, 50, −1, −0.5]	[100.96, 2.08, 1.80, **49.78**, −0.80, −0.57]	[99.62, 97.39, 93.18, **99.91**, 93.41, 97.67]	[1.79, 25.61, 9.31, **32.55**, 17.36, 4.42]
11	[100, 3, 1, 0, 0, 0]	[93.45, 3.01, 1.06, 2.19, 0.15, −0.01]	[97.38, 99.74, 97.97, 99.12, 94.88, 99.77]	[8.11, 1.54, 4.68, 5.10, 11.49, 1.97]
12	[100, 3, 2, 50, 1, −0.5]	[102.81, 2.94, 1.95, **50.88**, 1.04, −0.49]	[98.87, 98.18, 98.44, **99.65**, 98.62, 99.76]	[2.74, 14.85, 7.41, **39.79**, 12.51, 3.91]
13	[200, 1, 1, 0, −1, −1]	[199.61, 1.20, 1.00, 2.11, −0.81, −0.97]	[99.85, 93.71, 99.95, 99.16, 93.65, 99.10]	[1.79, 16.44, 3.85, 1.82, 9.21, 2.67]
14	[200, 1, 2, 0, 1, 0]	[199.71, 1.01, 1.96, 2.83, 1.23, 0.00]	[99.88, 99.72, 98.75, 98.87, 92.39, 99.97]	[8.04, 2.85, 3.15, 8.43, 38.17, 1.92]
15	[200, 2, 1, 0, 0, −0.5]	[199.85, 2.12, 0.96, 0.82, 0.06, −0.54]	[99.94, 96.32, 98.58, 99.67, 98.07, 98.59]	[0.79, 6.07, 4.19, 1.58, 7.07, 3.64]
16	[200, 2, 2, 0, −1, −0.5]	[199.50, 2.38, 1.89, −0.42, −0.92, −0.52]	[99.80, 88.23, 96.39, 99.83, 97.47, 99.24]	[1.69, 14.09, 6.02, 1.60, 10.61, 2.82]
17	[200, 3, 1, 0, 0, 0]	[199.58, 3.01, 1.00, 0.08, 0.14, −0.02]	[99.83, 99.56, 99.99, 99.97, 95.38, 99.38]	[1.22, 1.80, 4.38, 2.76, 14.93, 2.49]
18	[200, 3, 2, 0, 1, −0.5]	[201.15, 3.00, 1.97, 3.68, 0.94, −0.50]	[99.54, 99.91, 98.85, 98.53, 98.06, 99.90]	[8.69, 9.69, 5.26, 8.75, 10.69, 2.72]

Appendix B

Table 12
A summary of the ABC-SubSim inference results using U_{2S2} sensor measurement with variable sensing noise levels, for selected small damage cases with $\ell = 25$ [mm].

Case	θ [mm]	θ_{MAP} [mm]	η (%)	ξ (%)
		Noise level = 0%		
1	[25, 1, 1, −75, −1, −1]	[24.45, 1.62, 0.98, −74.61, −0.78, −0.91]	[99.78, 80.59, 99.38, 99.84, 92.58, 96.84]	[0.67, 15.15, 4.70, 0.51, 9.14, 5.74]
2	[25, 1, 2, 0, 1, 0]	[25.57, 1.02, 1.95, −0.88, 1.20, 0.13]	[99.77, 99.53, 98.42, 99.65, 93.32, 95.70]	[1.00, 5.49, 5.77, 0.75, 12.31, 13.87]
3	[25, 2, 1, −50, 0, −0.5]	[25.05, 2.03, 1.05, −49.78, −0.06, −0.47]	[99.98, 99.03, 98.44, 99.91, 98.10, 98.92]	[0.50, 6.40, 4.45, 0.72, 7.87, 6.63]
4	[25, 2, 2, 50, −1, −0.5]	[25.79, 1.99, 2.26, 52.44, −1.06, −0.34]	[99.68, 99.57, 91.27, 99.02, 97.88, 94.59]	[0.77, 15.93, 7.22, 0.84, 16.16, 3.67]
5	[25, 3, 1, 0, 0, 0]	[24.57, 3.04, 1.56, −0.13, −0.03, 0.06]	[99.83, 98.68, 81.27, 99.95, 98.96, 97.92]	[1.25, 3.58, 21.80, 1.27, 33.54, 6.83]
6	[25, 3, 2, 50, 1, −0.5]	[25.42, 2.67, 1.90, 50.88, 0.48, −0.33]	[99.83, 89.76, 96.70, 99.65, 82.55, 94.44]	[1.25, 12.66, 7.67, 1.12, 22.95, 9.37]
		Noise level = 2%		
1	[25, 1, 1, −75, −1, −1]	[24.29, 1.65, 0.98, −74.65, −0.93, −0.87]	[99.72, 79.55, 99.27, 99.86, 97.57, 95.74]	[0.73, 16.10, 5.37, 0.60, 12.05, 6.03]
2	[25, 1, 2, 0, 1, 0]	[26.18, 1.01, 1.95, −0.52, 1.09, −0.23]	[99.53, 99.82, 98.49, 99.79, 97.15, 92.32]	[0.85, 4.95, 6.01, 0.65, 8.61, 11.50]
3	[25, 2, 1, −50, 0, −0.5]	[25.33, 2.01, 1.00, −49.71, −0.13, −0.46]	[99.87, 99.78, 99.97, 99.88, 95.57, 98.51]	[0.54, 5.49, 4.30, 0.67, 10.97, 6.32]
4	[25, 2, 2, 50, −1, −0.5]	[24.84, 2.12, 2.10, 53.00, −1.08, −0.38]	[99.94, 96.20, 96.53, 98.80, 97.43, 95.90]	[0.85, 20.09, 5.82, 0.88, 11.17, 3.63]
5	[25, 3, 1, 0, 0, 0]	[23.92, 3.03, 1.35, −1.15, 0.16, −0.07]	[99.57, 98.98, 88.31, 99.54, 94.71, 97.81]	[1.36, 3.62, 20.94, 1.35, 37.67, 7.42]
6	[25, 3, 2, 50, 1, −0.5]	[25.53, 2.75, 1.92, 50.7, 0.43, −0.25]	[99.79, 92.15, 97.23, 99.71, 81.04, 91.81]	[0.76, 7.72, 4.92, 0.93, 15.23, 7.83]
		Noise level = 3%		
1	[25, 1, 1, −75, −1, −1]	[24.20, 1.46, 1.02, −74.90, −0.96, −0.88]	[99.68, 85.61, 99.45, 99.96, 98.54, 95.97]	[0.64, 20.23, 4.61, 0.50, 9.13, 5.61]
2	[25, 1, 2, 0, 1, 0]	[26.72, 1.01, 1.93, −0.70, 1.25, −0.30]	[99.31, 99.57, 97.82, 99.72, 91.75, 90.04]	[1.05, 7.09, 6.31, 0.84, 13.05, 14.34]
3	[25, 2, 1, −50, 0, −0.5]	[25.34, 2.01, 1.03, −49.85, −0.05, −0.41]	[99.86, 99.73, 99.11, 99.94, 98.50, 96.94]	[0.49, 4.61, 3.67, 0.66, 8.58, 5.42]
4	[25, 2, 2, 50, −1, −0.5]	[25.9, 1.96, 2.16, 52.8, −1.01, −0.35]	[99.62, 98.68, 94.63, 98.88, 99.68, 95.07]	[0.82, 17.61, 7.46, 0.74, 13.71, 3.99]
5	[25, 3, 1, 0, 0, 0]	[24.41, 3.03, 1.41, −1.17, −0.03, −0.04]	[99.77, 98.91, 86.20, 99.53, 99.16, 98.73]	[0.77, 3.26, 13.08, 0.89, 10.97, 5.89]
6	[25, 3, 2, 50, 1, −0.5]	[25.45, 2.54, 1.90, 52.04, 0.17, −0.37]	[99.82, 85.68, 96.59, 99.18, 72.43, 95.68]	[1.51, 10.49, 8.74, 1.02, 27.04, 12.35]
		Noise level = 5%		
1	[25, 1, 1, −75, −1, −1]	[24.98, 1.85, 1.04, −74.93, −0.65, −0.92]	[99.99, 73.56, 98.68, 99.97, 88.34, 97.45]	[0.62, 20.14, 3.86, 0.49, 10.23, 4.40]
2	[25, 1, 2, 0, 1, 0]	[26.32, 1.15, 1.96, −0.8, 1.02, −0.34]	[99.47, 95.4, 98.55, 99.68, 99.2, 88.66]	[0.72, 7.03, 6.41, 0.62, 9.00, 8.50]
3	[25, 2, 1, −50, 0, −0.5]	[25.34, 2.14, 0.97, −49.46, −0.13, −0.61]	[99.86, 95.62, 99.06, 99.78, 95.54, 96.40]	[0.71, 7.88, 6.22, 0.85, 7.30, 6.40]
4	[25, 2, 2, 50, −1, −0.5]	[26.11, 1.92, 2.16, 52.96, −1.04, −0.32]	[99.56, 97.36, 94.53, 98.81, 98.65, 93.89]	[0.83, 23.20, 8.72, 0.80, 16.14, 4.83]
5	[25, 3, 1, 0, 0, 0]	[26.62, 3.05, 2.20, 11.58, 1.22, −0.19]	[99.35, 98.43, 60.12, 95.37, 59.44, 93.63]	[1.46, 27.08, 43.99, 5.06, 31.95, 8.96]
6	[25, 3, 2, 50, 1, −0.5]	[24.97, 2.66, 1.84, 53.88, 0.43, −0.48]	[99.99, 89.45, 94.58, 98.45, 80.99, 99.41]	[2.55, 13.61, 14.27, 1.56, 38.15, 11.15]
		Noise level = 10%		
1	[25, 1, 1, −75, −1, −1]	[25.19, 2.05, 1.09, −74.72,−0.40, −0.87]	[99.92, 67.30, 96.99, 99.89, 80.02, 95.71]	[0.59, 15.14, 3.35, 0.47, 12.19, 4.26]
2	[25, 1, 2, 0, 1, 0]	[28.08, 1.05, 2.14, −1.29, 0.64, −0.20]	[98.77, 98.29, 95.49, 99.48, 87.87, 93.37]	[0.79, 5.64, 5.48, 0.62, 7.71, 6.24]
3	[25, 2, 1, −50, 0, −0.5]	[24.76, 1.98, 1.03, −49.27, 0.20, −0.34]	[99.90, 99.34, 98.96, 99.71, 93.37, 94.54]	[0.57, 6.40, 5.30, 0.75, 12.16, 7.72]
4	[25, 2, 2, 50, −1, −0.5]	[24.50, 1.97, 2.09, 51.23, −0.89, −0.41]	[99.80, 99.20, 96.98, 99.51, 96.40, 97.04]	[0.84, 32.88, 7.98, 2.05, 17.46, 4.90]
5	[25, 3, 1, 0, 0, 0]	[23.37, 3.05, 1.04, −1.58, 1.27, −0.09]	[99.35, 98.40, 98.60, 99.37, 57.58, 96.92]	[1.89, 2.74, 14.22, 1.57, 31.39, 5.74]
6	[25, 3, 2, 50, 1, −0.5]	[26.09, 2.82, 2.11, 52.73, 0.77, −0.17]	[99.56, 94.52, 96.34, 98.91, 92.31, 89.05]	[0.72, 7.31, 5.69, 0.99, 13.01, 7.56]

Table 13
A summary of the ABC-SubSim inference results using U_{2S2} sensor measurement with variable sensing noise levels, for selected large damage cases with $\ell = 200$ [mm].

Case	θ [mm]	θ_{MAP} [mm]	η (%)	ξ (%)
Noise level = 0%				
13	[200, 1, 1, 0, −1, −1]	[210.27, 0.99, 0.99, 3.14, −0.95, −0.98]	[95.89, 99.78, 99.69, 98.74, 98.42, 99.47]	[5.33, 21.08, 3.40, 2.77, 6.68, 2.27]
14	[200, 1, 2, 0, 1, 0]	[200.37, 1.03, 1.97, 0.57, 0.89, 0.02]	[99.85, 99.17, 99.06, 99.77, 96.35, 99.39]	[2.89, 1.96, 2.34, 1.46, 5.89, 3.26]
15	[200, 2, 1, 0, 0, −0.5]	[199.39, 2.06, 1.01, −1.82, −0.04, −0.51]	[99.76, 98.06, 99.70, 99.27, 98.54, 99.58]	[3.43, 3.13, 1.87, 2.10, 3.88, 3.73]
16	[200, 2, 2, 0, −1, −0.5]	[199.76, 2.10, 1.95, 0.23, −1.04, −0.49]	[99.91, 96.89, 98.45, 99.91, 98.57, 99.51]	[2.31, 11.11, 5.45, 1.29, 6.44, 3.41]
17	[200, 3, 1, 0, 0, 0]	[203.21, 3.00, 1.02, −0.82, 0.07, −0.00]	[98.72, 99.93, 99.30, 99.67, 97.70, 99.97]	[9.18, 1.56, 6.13, 3.99, 18.05, 4.49]
18	[200, 3, 2, 0, 1, −0.5]	[196.97, 3.00, 1.96, −0.22, 0.98, −0.47]	[98.79, 99.89, 98.62, 99.91, 99.32, 99.06]	[3.25, 3.15, 4.02, 1.58, 10.41, 2.80]
Noise level = 2%				
13	[200, 1, 1, 0, −1, −1]	[206.42, 1.49, 0.99, 2.70, −0.91, −0.98]	[97.43, 84.76, 99.55, 98.92, 96.84, 99.31]	[4.25, 18.77, 3.70, 2.34, 6.99, 2.43]
14	[200, 1, 2, 0, 1, 0]	[204.45, 1.03, 1.97, 1.54, 0.94, −0.04]	[98.22, 98.92, 98.90, 99.38, 97.97, 98.80]	[3.07, 2.17, 2.47, 1.65, 6.13, 3.39]
15	[200, 2, 1, 0, 0, −0.5]	[201.11, 2.06, 1.01, −1.67, −0.08, −0.52]	[99.55, 98.10, 99.77, 99.33, 97.45, 99.41]	[3.62, 3.43, 2.05, 2.17, 4.52, 4.14]
16	[200, 2, 2, 0, −1, −0.5]	[196.11, 2.23, 1.97, 0.72, −1.04, −0.49]	[98.44, 92.72, 98.92, 99.71, 98.51, 99.64]	[2.69, 10.50, 5.19, 1.28, 6.01, 3.34]
17	[200, 3, 1, 0, 0, 0]	[203.14, 3.01, 1.09, 1.72, −0.18, 0.04]	[98.74, 99.66, 97.09, 99.31, 94.12, 98.70]	[11.75, 1.70, 5.94, 5.25, 17.80, 4.92]
18	[200, 3, 2, 0, 1, −0.5]	[201.57, 3.00, 1.96, −0.12, 0.88, −0.46]	[99.37, 99.91, 98.69, 99.95, 96.09, 98.52]	[3.01, 3.15, 4.45, 1.65, 9.25, 2.91]
Noise level = 3%				
13	[200, 1, 1, 0, −1, −1]	[202.66, 0.94, 0.98, 2.52, −0.95, −0.96]	[98.94, 98.13, 99.19, 98.99, 98.32, 98.63]	[4.76, 23.22, 4.07, 2.49, 6.35, 2.39]
14	[200, 1, 2, 0, 1, 0]	[200.52, 1.02, 1.96, 0.73, 0.91, 0.03]	[99.79, 99.24, 98.56, 99.71, 97.00, 98.94]	[3.53, 2.20, 2.69, 1.75, 7.31, 3.69]
15	[200, 2, 1, 0, 0, −0.5]	[197.60, 2.06, 1.01, −1.95, −0.08, −0.52]	[99.04, 97.98, 99.66, 99.22, 97.41, 99.25]	[3.33, 2.90, 1.74, 2.05, 3.70, 3.49]
16	[200, 2, 2, 0, −1, −0.5]	[198.36, 2.13, 2.00, 0.59, −1.05, −0.46]	[99.35, 95.97, 99.92, 99.77, 98.17, 98.52]	[2.08, 7.75, 5.01, 1.05, 5.48, 3.21]
17	[200, 3, 1, 0, 0, 0]	[194.19, 3.00, 1.02, −3.42, 0.24, 0.03]	[97.68, 99.96, 99.44, 98.63, 92.03, 99.11]	[10.16, 1.63, 5.75, 4.81, 20.26, 4.75]
18	[200, 3, 2, 0, 1, −0.5]	[199.99, 2.97, 1.99, −0.12, 0.95, −0.44]	[100.0, 98.96, 99.55, 99.95, 98.45, 97.98]	[2.86, 3.08, 4.07, 1.47, 9.33, 2.60]
Noise level = 5%				
13	[200, 1, 1, 0, −1, −1]	[205.65, 1.61, 0.98, 1.91, −0.94, −0.98]	[97.74, 81.07, 99.29, 99.23, 97.84, 99.35]	[5.19, 21.68, 3.71, 2.62, 7.38, 2.36]
14	[200, 1, 2, 0, 1, 0]	[202.18, 1.02, 1.98, 1.52, 0.85, 0.00]	[99.13, 99.42, 99.29, 99.39, 94.88, 99.88]	[2.76, 1.95, 2.34, 1.56, 5.90, 3.19]
15	[200, 2, 1, 0, 0, −0.5]	[200.78, 2.07, 1.00, −1.21, −0.07, −0.53]	[99.69, 97.85, 99.92, 99.51, 97.82, 98.85]	[3.06, 2.76, 1.72, 1.81, 3.29, 3.08]
16	[200, 2, 2, 0, −1, −0.5]	[198.88, 2.18, 2.01, −0.12, −1.03, −0.47]	[99.55, 94.44, 99.58, 99.95, 98.87, 99.09]	[2.19, 7.12, 4.61, 1.13, 5.68, 2.80]
17	[200, 3, 1, 0, 0, 0]	[194.67, 3.02, 1.02, −0.63, 0.12, 0.04]	[97.87, 99.51, 99.27, 99.75, 96.02, 98.57]	[10.25, 1.57, 5.53, 5.01, 19.15, 4.46]
18	[200, 3, 2, 0, 1, −0.5]	[197.34, 2.98, 1.94, 0.12, 0.93, −0.46]	[98.94, 99.47, 98.10, 99.95, 97.82, 98.58]	[3.46, 3.24, 4.31, 1.77, 9.94, 3.06]
Noise level = 10%				
13	[200, 1, 1, 0, −1, −1]	[198.58, 2.07, 0.92, −0.06, −0.99, −1.00]	[99.43, 66.67, 97.36, 99.97, 99.75, 99.91]	[6.87, 32.13, 4.06, 3.18, 5.81, 2.30]
14	[200, 1, 2, 0, 1, 0]	[202.96, 1.03, 1.98, 0.13, 0.90, −0.02]	[98.82, 99.16, 99.34, 99.95, 96.65, 99.48]	[3.23, 2.18, 2.82, 1.84, 7.72, 3.42]
15	[200, 2, 1, 0, 0, −0.5]	[193.30, 2.10, 0.99, −4.85, 0.03, −0.54]	[97.32, 96.96, 99.52, 98.06, 98.86, 98.66]	[5.11, 2.64, 1.79, 2.73, 3.36, 3.00]
16	[200, 2, 2, 0, −1, −0.5]	[198.35, 2.18, 2.00, −0.08, −1.04, −0.47]	[99.34, 94.30, 99.91, 99.97, 98.72, 98.83]	[1.86, 6.24, 4.10, 0.92, 5.26, 2.57]
17	[200, 3, 1, 0, 0, 0]	[195.92, 2.99, 1.01, 1.85, −0.10, 0.05]	[98.37, 99.80, 99.69, 99.26, 96.75, 98.49]	[9.67, 1.71, 6.05, 5.11, 22.02, 4.47]
18	[200, 3, 2, 0, 1, −0.5]	[204.21, 2.98, 1.93, 1.54, 0.84, −0.48]	[98.32, 99.36, 97.80, 99.38, 94.60, 99.28]	[2.98, 3.06, 4.20, 1.73, 9.82, 2.47]

References

[1] Li Y, Wei Z, Wang Z, Li Y. Friction self-piercing riveting of aluminum alloy AA6061-T6 to magnesium alloy AZ31B. J Manuf Sci Eng 2013;135(6).

[2] Borrisutthekul R, Miyashita Y, Mutoh Y. Dissimilar material laser welding between magnesium alloy AZ31B and aluminum alloy A5052-O. Sci Technol Adv Mater 2005;6(2):199.

[3] Liu L, Liu X, Liu S. Microstructure of laser-tig hybrid welds of dissimilar Mg alloy and Al alloy with Ce as interlayer. Scripta Mater 2006;55(4):383–6.

[4] Haghshenas M, Gerlich A. Joining of automotive sheet materials by friction-based welding methods: a review, Engineering Science and Technology. Int J 2018;21(1): 130–48.

[5] Ostachowicz W, Kudela P, Krawczuk M, Zak A. Guided waves in structures for SHM: the time-domain spectral element method. John Wiley & Sons; 2011.

[6] Farrar CR, Lieven NA. Damage prognosis: the future of structural health monitoring. Phil Trans Math Phys Eng Sci 2007;365(1851):623–32.
[7] Park MH, Kim IS, Yoon YK. Ultrasonic inspection of long steel pipes using lamb waves. NDT E Int 1996;29(1):13–20.
[8] Fakih MA, Mustapha S, Tarraf J, Ayoub G, Hamade R. Detection and assessment of flaws in friction stir welded joints using ultrasonic guided waves: experimental and finite element analysis. Mech Syst Signal Process 2018;101:516–34.
[9] Ismail Z, Mustapha S, Fakih MA, Tarhini H. Sensor placement optimization on complex and large metallic and composite structures. Struct Health Monit 2020;19 (1):262–80.
[10] Fakih MA, Mustapha S, Makki Alamdari M, Ye L. Symbolic dynamics time series analysis for assessment of barely visible indentation damage in composite sandwich structures based on guided waves. J Compos Mater 2017;51(29): 4129–43.
[11] Fakih MA, Mustapha S, Abdul-Aziz A. Robust localization and classification of barely visible indentations in composite structures by fusion of ultrasonic damage indices. J Nondestr Eval Diagn Prognostics Eng Syst 2019;2(3).
[12] Rose JL. Ultrasonic guided waves in solid media. Cambridge university press; 2014.
[13] Su Z, Ye L. Identification of damage using Lamb waves: from fundamentals to applications, vol. 48. Springer Science & Business Media; 2009.
[14] Tarhini H, Itani R, Fakih MA, Mustapha S. Optimization of piezoelectric wafer placement for structural health-monitoring applications. J Intell Mater Syst Struct 2018;29(19):3758–73.
[15] Ismail Z, Fakih MAH, Mustapha SA, Tarhini HA. The application of genetic algorithm for sensor placement of PZT wafer towards the application in structural health monitoring. In: 12th European conference on non-destructive testing (ENCDT), vol. 13. Gothenberg; 2018.
[16] Cantero-Chinchilla S, Chiachío J, Chiachío M, Chronopoulos D, Jones A. A robust Bayesian methodology for damage localization in plate-like structures using ultrasonic guided-waves. Mech Syst Signal Process 2019;122:192–205.
[17] Cantero-Chinchilla S, Chiachío J, Chiachío M, Chronopoulos D, Jones A. Optimal sensor configuration for ultrasonic guided-wave inspection based on value of information. Mech Syst Signal Process 2020;135:106377.
[18] Cantero-Chinchilla S, Beck JL, Chiachío M, Chiachío J, Chronopoulos D, Jones A. Optimal sensor and actuator placement for structural health monitoring via an efficient convex cost-benefit optimization. Mech Syst Signal Process 2020;144: 106901.
[19] Sbarufatti C, Manson G, Worden K. A numerically-enhanced machine learning approach to damage diagnosis using a Lamb wave sensing network. J Sound Vib 2014;333(19):4499–525.
[20] Marin J-M, Pudlo P, Robert CP, Ryder RJ. Approximate Bayesian computational methods. Stat Comput 2012;22(6):1167–80.
[21] Salehi H, Burgueño R. Emerging artificial intelligence methods in structural engineering. Eng Struct 2018;171:170–89.
[22] Chiachio M, Beck JL, Chiachio J, Rus G. Approximate Bayesian computation by subset simulation. SIAM J Sci Comput 2014;36(3):A1339–58.
[23] Su Z, Ye L. Lamb wave propagation-based damage identification for quasi-isotropic cf/ep composite laminates using artificial neural algorithm: Part i-methodology and database development. J Intell Mater Syst Struct 2005;16(2):97–111.
[24] Su Z, Ye L. Lamb wave propagation-based damage identification for quasi-isotropic cf/ep composite laminates using artificial neural algorithm: Part ii implementation and validation. J Intell Mater Syst Struct 2005;16(2):113–25.
[25] Lu Y, Ye L, Su Z, Zhou L, Cheng L. Artificial neural network (ann)-based crack identification in aluminum plates with Lamb wave signals. J Intell Mater Syst Struct 2009;20(1):39–49.
[26] Alleyne DN, Cawley P. A 2-dimensional Fourier transform method for the quantitative measurement of Lamb modes. In: IEEE symposium on ultrasonics. IEEE; 1990. p. 1143–6.
[27] Alleyne D, Cawley P. A two-dimensional Fourier transform method for the measurement of propagating multimode signals. J Acoust Soc Am 1991;89(3): 1159–68.
[28] Song F, Huang G, Hudson K. Guided wave propagation in honeycomb sandwich structures using a piezoelectric actuator/sensor system. Smart Mater Struct 2009; 18(12):125007.
[29] Mustapha S, Ye L. Leaky and non-leaky behaviours of guided waves in CF/EP sandwich structures. Wave Motion 2014;51(6):905–18.
[30] Pan N, Su Z, Ye L, Zhou L-M, Lu Y. A quantitative identification approach for delamination in laminated composite beams using digital damage fingerprints (DDFs). Compos Struct 2006;75(1–4):559–70.
[31] Tarraf J, Mustapha S, Fakih MA, Harb M, Wang H, Ayoub G, Hamade R. Application of ultrasonic waves towards the inspection of similar and dissimilar friction stir welded joints. J Mater Process Technol 2018;255:570–83.
[32] Fakih MA, Mustapha S, Harb M, Ng C-T. Understanding the interaction of the fundamental lamb-wave modes with material discontinuity: finite element analysis and experimental validation. Structural Health Monitoring; 2021. 14759217211007118.
[33] Papazafeiropoulos G, Muñiz-Calvente M, Martínez-Pañeda E. *Abaqus2Matlab*: a suitable tool for finite element post-processing. Adv Eng Software 2017;105:9–16.
[34] Fakih M, Mustapha S, Harb M. The interaction of the fundamental symmetric and antisymmetric lamb wave modes with material discontinuity: a 3D finite element analysis. In: Proceedings of the 7th Asia Pacific workshop on structural health monitoring (APWSHM). Hong Kong, China: SHM; 2018.
[35] Brownlee J. Discover how they work and implement them from scratch. 2016.
[36] Kohavi R, et al. A study of cross-validation and bootstrap for accuracy estimation and model selection. In: Ijcai, vol. 14. Montreal: Canada; 1995. p. 1137–45.
[37] Møller MF. A scaled conjugate gradient algorithm for fast supervised learning. Neural Network 1993;6(4):525–33.
[38] Beck JL. Bayesian system identification based on probability logic. Struct Control Health Monit 2010;17(7):825–47.
[39] Marjoram P, Molitor J, Plagnol V, Tavare S. Markov chain Monte Carlo without likelihoods. Proc Natl Acad Sci Unit States Am 2003;100(26):15324–8.
[40] Fearnhead P, Prangle D. Constructing summary statistics for approximate Bayesian computation: semi-automatic approximate Bayesian computation. J Roy Stat Soc B 2012;74(3):419–74.
[41] Au S-K, Beck JL. Estimation of small failure probabilities in high dimensions by subset simulation. Probabilist Eng Mech 2001;16(4):263–77.
[42] Zuev KM, Beck JL, Au S-K, Katafygiotis LS. Bayesian post-processor and other enhancements of subset simulation for estimating failure probabilities in high dimensions. Comput Struct 2012;92:283–96.
[43] Gardner P, Bull L, Dervilis N, Worden K. Overcoming the problem of repair in structural health monitoring: metric-informed transfer learning. J Sound Vib 2021: 116245.